Front propagation in a laminar cellular flow: Shapes, velocities, and least time criterion

A. Pocheau* and F. Harambat

IRPHE, CNRS & Universités Aix-Marseille I & II, 49 rue Joliot-Curie, B.P. 146, Technopôle de Château-Gombert, F-13384 Marseille, Cedex 13, France

(Received 22 June 2007; revised manuscript received 17 October 2007; published 7 March 2008)

We experimentally investigate the propagation of chemical fronts in steady laminar cellular flows at large Péclet numbers and large Damköhler numbers. Fronts are generated in an aqueous solution by an autocatalytic oxydoreduction reaction. They propagate in a channel in which a chain of counter-rotative parallel vortices is induced by electroconvection. We first accurately determine the form, the dynamics and the mean velocity of these fronts in the whole Hele-Shaw regime of the flow. We then address the modeling of the evolution of their mean velocity with the flow amplitude. The structure of the front wakes yields us to reject an effective reaction-diffusion wave as a relevant model for large-scale front propagation. On the other hand, analysis of the role of front heads brings us to introduce a kinematic model at the vortex scale for uncovering the front dynamics. This model addresses the propagation of the front leading point in a chain of vortices whose field is modeled by a two-dimensional solid rotation complemented by a boundary layer. Interestingly, it sensitively relies on the effective trajectory followed by the front leading point. To account for this, a competition is worked out among a one-parameter family of potential trajectories. The actual trajectory is then selected as the fastest one with quite a good agreement with measurements and observations. In particular, the measured effective front velocities are well recovered from the model, including their intrinsic dependence on the boundary layer width. Accordingly, effective front propagation in a laminar steadily stirred medium is thus understood from an optimization principle similar to the Fermat principle of ray propagation in heterogeneous media.

DOI: 10.1103/PhysRevE.77.036304 PACS number(s): 47.70.Fw, 82.40.Ck, 45.10.Db

I. INTRODUCTION

Propagation of a front in a stirred medium encompasses a large variety of topics ranging from chemistry [1,2], combustion [3], epidemics [4], to marine ecology [5,6] or ozone depletion [7]. It thus stands as a canonical transport process which involves both fundamental and industrial implications in physics, chemistry, or environment and which has motivated a number of works in applied mathematics [8,9]. Its main originality consists in confronting, within the same system, two different kinds of transport phenomena: a nonlinear reaction-diffusion process, following which a metastable or unstable state is progressively transformed into a stable state, and an advective, passive transport process by vortex stirring and mixing, following which concentration fields are progressively diffused and homogenized. Whereas the former mechanism tends to produce steep gradients, the latter aims at smoothing them. Altogether, they give rise to an effective reactive transport by convoluted fronts which sets a compromise between a sharp phase transformation and a large range homogenization.

Needless to say, recovering the main features of the resulting balance between such antagonist phenomena calls for a fine modeling of their spatial and temporal mechanisms. What makes this delicate task valuable is the significant changes of shape and velocity displayed by propagative fronts and the resulting important practical implications. In particular, one of its most popular application refers to internal combustion engines in which the improvement of the effective propagation of a reactive front by turbulent flows currently serves to raise cycle frequencies and, therefore, the resulting car velocities. Other implications that involve laminar flows may address propagation in porous media or in confined systems, possibly even including microfluidic devices.

In contrast with turbulent propagation [3,10,11], front propagation in laminar flows involves a coherence and a steadiness of the medium following which a long time, large scale correlation between the flow pattern and the effective front propagation can set in. In this context, a central question refers to the existence of significant open streamlines. If there is some, front propagation will likely benefit from flow advection on these lines. On the opposite, in case of closed streamlines and thus of cellular flows, front propagation will be unable to use flow advection on a long range. Its effective propagation will then correspond to a compromise between enhanced propagation within vortices and slow transport across vortex boundaries. From this balance, an abnormal type of transport, in between advection and reaction-diffusion, may be expected.

The present study addresses front propagation in steady cellular flows. Its objectives are twofold: first, document this issue experimentally, then develop an efficient modeling built on observed features and suitable for extension to more complex configurations.

Transport in cellular flows has been reported in literature for a passive tracer. At large Péclet number and at large times compared to the diffusive time scale, the tracer was found to spread over a large number of cells. Its concentration then displayed a diffusive profile that was set on a scale large compared to the cell scale [12]. This profile was found to satisfy an effective diffusion equation derived by renormal-

*alain.pocheau@irphe.univ-mrs.fr

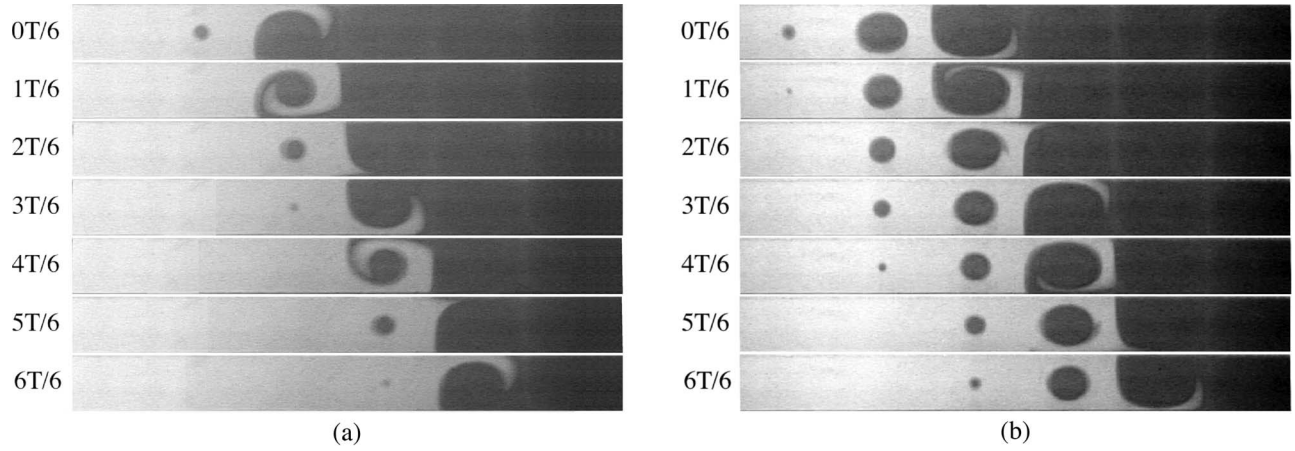

FIG. 1. Colorless front propagating from left to right in the vortex chain of the 12 mm large channel. Images correspond to different instants of propagation over a period T. From the upper image to the lower one: $t=0$, $T/6$, $2T/6$, $3T/6$, $4T/6$, $5T/6$, $6T/6$. (a) Moderate advection: $U/V_o=9.0$, $V_f/V_o=5.4$. (b) Larger advection: $U/V_o=18.8$, $V_f/V_o=7.8$.

ization of the advection-diffusion equation at a scale large compared to the cell scale [13,14]. The resulting effective diffusivity was then found to be proportional to both the molecular diffusivity and the square root of the Péclet number [13,14], in agreement with experiments [15]. There, the difficulty in crossing cell boundaries by tracer diffusion was handled by a dependence on the Péclet number. In our configuration, a similar slowing down of front propagation in the vicinity of cell frontiers is expected to reduce the effective front velocity in a way that remains to be experimentally determined and modeled.

We report here a detailed experimental study of propagation of a reaction front in a steady cellular flow [16]. The experimental configuration has been designed so as to provide planar flows and thus the most appropriate conditions for a two-dimensional modeling. Fronts are produced by an autocatalytic reaction in an aqueous solution: the "chlorite-iodide" reaction. They involve a propagation velocity with respect to the fluid, the so-called laminar velocity, that we shall label V_o. Cellular flows have been generated by magnetohydrodynamic means [12], the solution being placed above an array of magnets and crossed by an electric current. Both the trajectories and the effective velocity V_f of the front have been studied as a function of the flow intensity U in the moderate flow velocity regime $U/V_o=O(10)$ where the flow is planar in the Hele-Shaw regime.

Observation of the front wake shows a discrete series of sharp, disconnected fronts (Fig. 1), which contrasts with the thickened fronts expected in the fast advection regime $U/V_o \gg 10$ (see Fig. 2 for large $\mathrm{Pe}/\xi \propto U/V_o$). This means that the model of effective reaction-diffusion wave derived for the latters [17–21] does not apply to the present regime. Instead, observation of front propagation in a vortex reveals definite trajectories of the front heads which call for a kinematic modeling. However, to account for the sensitivity of the resulting front velocity to the front trajectory, a competition between a family of potential trajectories has to be worked out. We implement it in a suitable one-parameter family by selecting the fastest trajectory as the actual trajectory. This provides quite a good agreement with both the measurements of effective front velocities and the detailed observations of front propagation in vortices.

Interestingly, the resulting front dynamics appears to depend not only on the flow magnitude but also on its structure, i.e., on the relative width of the boundary layer. This dependence on subscale structures is corroborated by comparison between experiments performed at different vortex aspect ratios. Altogether, these results provide a relevant modeling of front propagation in cellular flows at moderate amplitude. The corresponding model is based on an optimization principle similar to the least-time Fermat principle of light propagation but applied here to a heterogeneous medium made by vortices. Although worked out here on planar flows, its general formulation allows extensions to more complex flows.

The paper is organized as follows. Section II reviews the literature on front propagation in cellular flows. The experimental setup is described in Sec. III and the experimental results are reported in Sec. IV together with their analyses. They lead us to build in Sec. V a model of front propagation based on an optimization procedure among a suitable set of trajectories. This model is worked out in Sec. VI and validated in Sec. VII by comparison with experimental observations and measurements. A discussion about this work and the insights it gives on the mechanisms of front propagation in cellular flows is given in Sec. VIII. It is followed by a conclusion about this study.

II. FRONT PROPAGATION IN CELLULAR FLOWS: REGIMES, MODELS, AND SIMULATIONS

We review here the current knowledge on fronts propagating in a two-dimensional (2D) cellular flow. As our experiment stands in a Hele-Shaw regime, this flow will correspond in practice to the largest planar flow which composes the actual Poiseuille flow, i.e., the 2D flow displayed at middepth of the channel. We classify below the different regimes. We then report on the models proposed to date and on the relevant experimental observations.

For simplicity of the modeling, it is assumed that the evolution of the chemical reaction can be represented by a single

progress variable θ, $0 \leqslant \theta \leqslant 1$, linked to the concentration of products. We label $\mathbf{U}$ the velocity field of the flow in the barycentric fluid frame, θ the progress variable of the reaction in between the initial ($\theta=0$) and final ($\theta=1$) states, D the molecular diffusivity of species, τ their reaction time, and $f(\theta)/\tau$ their reaction rate. The evolution of the progress variable is then given by the advection-reaction-diffusion equation,

$$\partial_t \theta + \mathbf{U} \cdot \boldsymbol{\nabla} \theta = D \Delta \theta + \frac{f(\theta)}{\tau}. \tag{1}$$

Whereas function $f(\cdot)$ is positive, its shape depends on the nature of the reactive phenomenon. When a strong activation energy is involved, $f(\cdot)$ displays an Arrhenius-like nonlinearity: $f(\theta)=\exp(-\theta_a/\theta)P(\theta)$, where $P(\cdot)$ is a polynomial and θ_a the activation barrier. When the activation energy is negligible, $f(\cdot)$ then simply reduces to the polynomial $P(\cdot)$. Usually, it is assumed that the initial state $\theta=0$ is, as the final state $\theta=1$, a steady state: $P(0)=P(1)=0$. For the sake of simplicity, we shall restrict attention below to the case of convex $f(\cdot)$ [so-called Kolmogorov-Petrovskii-Piskunov (KPP) nonlinearity [22]].

A. Laminar front: $U=0$

In the absence of flow, $\mathbf{U}=\mathbf{0}$, the planar front velocity is known to crucially depend on the shape of function $f(\cdot)$. In the Arrhenius-like case, the reaction zone and the diffusion zone negligibly overlap so that flux conservation at their boundary simply succeeds in fixing the front velocity [23]. In the polynomial case, i.e., $\theta_a=0$, the reaction zone spreads all over the diffusion zone, so that both processes must be handled together. It then exists a continuous family of traveling wave solutions with front velocities V larger than a minimum V_m. This minimum corresponds to the linear spreading velocity, i.e., to the velocity that would display the front edge close to the fresh medium $\theta=0$ for a linearized reaction rate $f(\theta) \equiv f'(0)\theta$. However, for compact or steep enough initial conditions, a single nonlinear traveling-wave solution with a specific velocity V_o is selected beyond transients for dynamical reasons [22,24].

For convex reaction rates $f(\cdot)$, i.e., in the KPP case, the selected front velocity V_o corresponds to the linear spreading velocity V_m [22,24]:

$$V_o = 2f'(0)^{1/2}\left(\frac{D}{\tau}\right)^{1/2}. \tag{2}$$

As the front dynamics is set by the leading edge $\theta \approx 0$ close to the fresh medium, this case is referred to as a pulled dynamics [24].

When the reaction rate $f(\cdot)$ is not convex, its nonlinearities are essential for setting the selected front velocity. Then, V_o lies in between the previous value and the value $2\sqrt{FD/\tau}$ where $F=\max_{0\leqslant\theta\leqslant 1} f(\theta)/\theta > f'(0)$. For polynomial $f(\cdot)$, its definite value can be derived without explicitly solving for the front solution [25]. The fact that V_o is larger than the value (2) deduced from the sole analysis of the front edge $\theta \approx 0$ close to the fresh medium means that the front velocity is now set in the internal part of the front, in a region of finite θ. This case is then referred to as a pushed dynamics [24].

The front thickness λ corresponds to the characteristic size of the variation zone in between the two asymptots $\theta=0$, $\theta=1$. For dimensional reasons, it is of order $\sqrt{D\tau}$. In particular, defining it as the length required to connect the front asymptots with the closest linear profile, we obtain, for a symmetric profile, $\lambda=\theta'(M)^{-1}$ where M denotes the front middle point: $\theta(M)=1/2$ and $\theta''(M)=0$. This, together with Eq. (1), yields $\lambda=V_o\tau/f(1/2)$ and, in the KPP case (2),

$$\lambda = 2\frac{f'(0)^{1/2}}{f(1/2)}(D\tau)^{1/2}. \tag{3}$$

We shall refer hereafter to the relations (2) and (3) as the KPP solution. Notice that, as the dynamics of θ depends only on the reaction rate, i.e., on the ratio $f(\theta)/\tau$, an arbitrary normalization can be applied to the production term $f(\theta)$. It usually corresponds to the arbitrary specification, $f'(0)=1$. For the sake of simplicity, we shall adopt this convention in the remainder.

B. Cellular flow: $U>0$

When the front propagates in a cellular flow, two additional characteristic variables are in order: a typical flow intensity U and a typical vortex size L [see Fig. 3(b) with $L \approx L_x \approx L_y$]. One is therefore left with two characteristic sizes, λ, L, and three characteristic times, $\tau_r=\tau$, $\tau_a=L/U$, $\tau_d=L^2/D$, and thus with three nondimensional parameters: the Damköhler number $\mathrm{Da}=\tau_a/\tau_r=L/U\,1/\tau$, the Péclet number $\mathrm{Pe}=\tau_d/\tau_a=UL/D$, and the relative vortex size $\xi=L/\lambda$. Following Eq. (3), these nondimensional parameters are linked by the relationship

$$\mathrm{Pe}\,\mathrm{Da} = \frac{\tau_d}{\tau_r} = g\xi^2, \tag{4}$$

with $g=4f'(0)f(1/2)^{-2}$. In addition, the relative vortex intensity U/V_o writes, with $\tilde{g}=(1/4)\,f(1/2)/f'(0)$,

$$\frac{U}{V_o} = \frac{1}{2f'(0)^{1/2}}\frac{(\tau_d\tau_r)^{1/2}}{\tau_a} = \tilde{g}\frac{\mathrm{Pe}}{\xi}. \tag{5}$$

As the flow gradient is smooth in cellular flows, the maximal flow velocity can play the role of a typical flow intensity. This is especially true in the Hele-Shaw regime in which the present experiment will lay, since the geometry of the flow streamlines is then independent of the flow intensity. For these reasons, we shall refer hereafter to U as the maximal velocity of the 2D flow $\mathbf{U}$.

Different qualitative regimes may be identified depending on the above parameters. They are analyzed in Appendix A and reported in Fig. 2 on two equivalent diagrams, one in the (ξ, Da) coordinates and the other in the (Pe, Da) coordinates. They correspond to thin fronts that keep the same structure as laminar fronts or to thickened fronts whose thickness extends on several vortices. The former fronts refer to laminar fronts, wrinkled fronts called "flamelets" or disconnected fronts whose reaction zone is then distributed over several vortices. The thickened fronts refer to the so-called thick

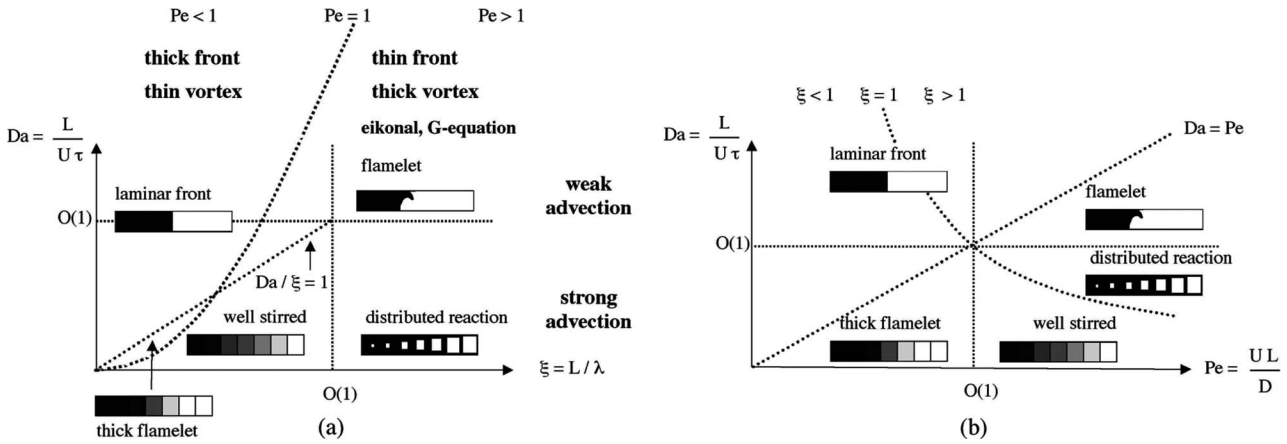

FIG. 2. Diagram of the different regimes of front propagation depending on the non-dimensional numbers (Pe, Da, ξ). The vortex size L is kept fixed but the front thickness λ is allowed to vary with $\xi = L/\lambda$. For reasons reported in Section II B, the different regimes are referred to laminar front, flamelet, thick flamelet, distributed reaction zone and well stirred regime. The present experiment stands in the large Péclet, large Damköhler and large relative vortex size regime, $\mathrm{Pe} \gg 1, \mathrm{Da} \gg 1, \xi \gg 1$, in which flamelets and eïkonal dynamics are expected. (a) Diagram coordinates (Da, ξ). Following (4), the iso-Péclet lines are parabolas. (b) Diagram coordinates (Da,Pe). Following (4), the iso-ξ lines are hyperbolas.

flamelets that may extend to the whole medium in the well-stirred regime.

C. Models and simulations

Whereas the small Péclet number regime has not attracted much attention due to the weakness of the expected effects of advection, various theoretical and numerical studies have been devoted to understanding the front behavior in the large Péclet number regime, for small or large Damköhler numbers Da and relative vortex size ξ [17–21]. Their goal has been to express the relationship between the relative enhancement of front velocity V_f/V_o and the relevant adimensional parameters (Pe, Da, ξ) of the system. We review their main conclusions below.

1. $\mathrm{Pe} \gg 1$, $\mathrm{Da} \ll 1$

This large Péclet, small Damköhler regime refers either to the well-stirred regime or to the distributed reaction zone regime [Fig. 2(b)]. It corresponds to a strong advection regime, $\tau_a \ll \tau_r$, for which advection at the vortex scale occurs before reaction is completed. It has been analyzed by phenomenological renormalization of the properties of the system at a scale large compared to the vortex size [17–19]. This approach turned out absorbing advection effects in an enhancement of the effective diffusion at large scale, in a way reminiscent of that undergone in a similar situation for a passive scalar [13,14].

In the renormalization framework, either the asymptotic coherence of the system behavior at large flow velocity [17] or the dimensional relationship of the effective reaction-diffusion velocity with the effective diffusivity [18,19] point to a definite power-law variation of the front velocity V_o with the flow amplitude U:

$$V_f/V_o \sim (U/V_o)^{1/4}. \tag{6}$$

Simulations based either on discrete-time maps [18,19] or on a direct method for KPP [18–20], Arrhenius [18,19], or ignition production rates [20] have confirmed this power-law dependence for propagation in a *two-dimensional* flow $\mathbf{U}$ with *free* boundary conditions [18–20],

$$\mathbf{U} = \boldsymbol{\nabla} \wedge (\psi \mathbf{z}); \quad \psi = UL/\pi \sin(\pi x/L)\sin(\pi y/L). \tag{7}$$

However, as front propagation is driven by *two* independent parameters among three, relation (6) is insufficient to identify by itself the respective role of each parameter (Pe, Da, ξ). In particular, renormalization approaches did not explicitly address the dependence on ξ [17–19], but further analysis of the role of the Damköhler number Da made two of them conclude to the following dependence on Pe and Da [18,19]:

$$\mathrm{Pe} \gg 1, \quad \mathrm{Da} \ll 1 : V_f/V_o \sim \mathrm{Pe}^{1/4}\,\mathrm{Da}^0.$$

On the other hand, numerical simulations by Vladimirova *et al.* evidenced a dependence on the relative vortex size ξ [20],

$$\mathrm{Pe} \gg 1, \quad \mathrm{Da} \ll 1 :$$

$$\xi \gg 1 : V_f/V_o \sim \xi^{3/4}(U/V_o)^{1/4}, \tag{8}$$

$$\xi \ll 1 : V_f/V_o \sim \xi^{1/4}(U/V_o)^{1/4}, \tag{9}$$

whose equivalent form

$$\mathrm{Pe} \gg 1, \quad \mathrm{Da} \ll 1 :$$

$$\xi \gg 1 : V_f/V_o \sim \mathrm{Pe}^{1/2}\,\mathrm{Da}^{1/4}, \tag{10}$$

$$\xi \ll 1 : V_f/V_o \sim \mathrm{Pe}^{1/4}\,\mathrm{Da}^0 \tag{11}$$

conflicts with Eq. (8) in the $\xi \gg 1$ regime. The origin of this discrepancy was identified in Ref. [20] as coming from a different evaluation of the characteristic scale on which gradients of concentration are built within a vortex.

2. Pe≫1, Da≫1

This large Péclet, large Damköhler regime refers to the flamelet regime [Fig. 2(b)]. It corresponds to a weak advection regime, $\tau_r \ll \tau_a$, for which reaction is completed before a fluid particle ends up a turn around a vortex. Following Eq. (4), the relative vortex size ξ is then necessarily large. This legitimates an eïkonal approximation following which, in the frame comoving with the flow, the front keeps the same inner structure as a laminar flow. Up to weak curvature effects, it thus advances with a normal front velocity in the frame of the flow. This kinematics can be modeled by a field equation, the G equation, for which the iso-G lines move with normal velocity V_o in the frame comoving with the flow field $\mathbf{U}$,

$$\partial_t G + \mathbf{U} \cdot \nabla G = V_o |\nabla G|.$$

In this so-called geometrical limit, the front then corresponds to an iso-G line which evolves according to the Huygens principle in this stirred medium.

The numerical simulations reported above in the small Da regime have been extended to this large Da regime for the same 2D cellular vortex flow (7) [18–21]. They revealed a convex variation of V_f/V_o with respect to U/V_o that was close to a power law with a 3/4 exponent. However, Vladimirova *et al.* evidenced no dependence on the relative vortex size ξ [20]:

$$\mathrm{Pe} \gg 1, \quad \mathrm{Da} \gg 1:$$

$$\xi \gg 1: V_f/V_o \sim \xi^0 (U/V_o)^{3/4} \tag{12}$$

$$\sim \mathrm{Pe}^{3/8}\, \mathrm{Da}^{-3/8}, \tag{13}$$

whereas the heuristical renormalization of the reaction-diffusion equation by Abel *et al.* [18,19] found some,

$$\mathrm{Pe} \gg 1, \quad \mathrm{Da} \gg 1:$$

$$\xi \gg 1: V_f/V_o \sim \mathrm{Pe}^{1/4}\, \mathrm{Da}^{-1/2}, \tag{14}$$

$$\sim \xi^{1/4} (U/V_o)^{3/4}. \tag{15}$$

This disagreement indicates that the identification of the proper scales on which renormalization must be built is a subtle task in this regime.

Turning attention to kinematics, Abel *et al.* [19] and Cencini *et al.* [21] have then proposed a modeling of the displacement of the front tip (Sec. V B) that provided the following relationship for its averaged velocity:

$$\frac{V_f}{V_o} = \frac{\pi}{2} \frac{\sqrt{(\beta U/V_o)^2 - 1}}{\ln[\beta U/V_o + \sqrt{(\beta U/V_o)^2 - 1}]}. \tag{16}$$

Here β is a numerical coefficient which averages the effect of the two-dimensional nature of the flow. As noticed by Vladimirova *et al.*, the relationship (16) and the power-law behavior (12) are too close to be distinguished [20].

The relationship (16) was also considered by Vladimirova *et al.* as the effective velocity of a front propagating along the separatrixes [20]. On these particular trajectories, the effective value of β was strictly unity. However, the two-dimensional nature of the issue was reflected in the fact that the path to follow was twice longer as in the above model. This was because the separatrix on the y axis had to be followed to proceed propagation on the x axis in the next vortex. Then, the predicted result was only *half* the effective velocity observed in simulations.

D. Experiments

Experiments on front propagation in flows have mostly addressed turbulent flows [26–28], Poiseuille flows [29], or flows induced by Rayleigh-Taylor [30–33] or Marangoni instability [34–36]. They thus referred to multiscale forced flows or to self-generated flows coupled to the front dynamics. In between, there remains important issues referring to front propagation in coherent forced flows involving few scales. They raise the difficulty of finely controlling the spatial or temporal features of flows during front propagation. Few experiments have been devoted to address them [28,37,38].

The most detailed experiment on front propagation in coherent flows has consisted in spatially modulating the amplitude of a parallel flow by a periodic chain of cylindric bluff bodies [37]. It has then succeeded in quantitatively determining the response of the front to the modulations. However, being conducted in gaseous combustion, it involved gas expansion and thus a feedback of the front dynamics on the flow features. This makes it difficult to extrapolate its results to more athermic reactions. In addition, it addressed a shear flow that contrasts with the cellular vortex flow that we wish to study here.

Two other experiments have involved autocatalytic fronts [28,38]. As the former experiment was intended to investigate a turbulent regime in a Taylor-Vortex flow [28], it involved a wide range of flow intensity over which flow transitions and stretch effect of the front by the flow could arise. On a smaller range of relative flow intensities, similar to that studied here, it provided few data points that seem to indicate an increase of effective front velocity with flow intensity more than linear, in contrast with the results reported below. A possible origin for this difference could be either a transition to time-dependent Taylor-Couette flow or a large scale flow, both of them improving front propagation. As the latter experiment was devoted to front propagation in an oscillating annular vortex chain [38], it provided few measurements of effective front velocity in a steady vortex chain. Its data are, however, consistent with an effective front velocity increasing with flow intensity less than linearly, in qualitative agreement with our findings below. They also exhibit quantitative differences that probably refer to differences in boundary conditions and in relative fluid depth.

III. EXPERIMENT

The experiment is designed so as to provide a controlled, reproducible cellular flow organized on a one-dimensional pattern. For this a chain of alternating vortices is generated by electromagnetic means in a narrow depth channel so as to remain in the Hele-Shaw regime. A propagating front is then

induced by ignition of an autocalytic reaction. This results in a model experiment of front propagation in a planar cellular flow.

We label $\mathbf{V}(x,y,z)$ the actual flow and $\mathbf{U}(x,y)$ the 2D flow that corresponds to the maximal value of $\mathbf{V}$ on the channel depth z. In the present Hele-Shaw regime, this flow will be found at the middepth of the channel: $\mathbf{U}(x,y)=\mathbf{V}(x,y,d/2)$. In agreement with the definition adopted in models (Sec. II), we shall then denote U the maximal velocity of this flow $\mathbf{U}(x,y)$ on a vortex.

The relevant parameters of the experiment are $D\approx 2\times 10^{-9}$ m^2 s^{-1}, $V_o\approx 2$ mm min^{-1}, $L=20$ mm, $3<U<35$ mm min^{-1} and, as shown in Sec. III E, $\tau=7$ s, $\lambda=1$ mm. They yield the following ranges of nondimensional parameters: $500<\mathrm{Pe}<5800$, $5<\mathrm{Da}<60$, and $\xi\approx 20$. This corresponds to the large Péclet, thin front, and weak advection regime, i.e., the flamelet regime, in which the front displays the same local structure as in the laminar case but a complex global geometry (Fig. 2).

A. Experimental configuration

The chemical solution is introduced in a long, narrow, and thin rectangular channel whose length X, width L_y and depth d are $X=20$cm, $L_y=12$mm or 6mm, $d=3$mm. (Fig. 3). This channel is built with horizontal top and bottom glass plates, 3 mm thick, which sandwich a rectangular plexiglass cell. The lower horizontal glass plate involves a mirror face for visualization from above. Except from Fig. 4(b), all the images reported below will thus correspond to top views of the channel.

A series of magnets, 20 mm long and 30 mm large, is placed below the lower plate to allow electroconvection. Their vertical magnetic field B is aligned along the depth direction but displays alternating orientations [Fig. 3(a)]. This results in a chain of up and down magnetic fields which are nearly homogeneous on each magnet but which involve large gradients at the magnet boundaries. As the extent of the magnetic field on the depth direction of the set-up is small, about 4 to 5 mm, care had to be taken to use a fluid layer thin enough to ensure a nearly homogenous Laplace force on its depth. In practice, a fluid depth d of 3 mm was adopted.

As the solution is ionic, an electric current I of a few mA can be generated by two electrodes placed at the extremities of the channel and submitted to an applied voltage difference of 15 V at most. This current gave rise to a density of Laplace forces $\mathbf{f}\approx\mathbf{j}\wedge\mathbf{B}$ where $\mathbf{j}$, the current density, was at the dominant order uniform $\mathbf{j}\approx IL_y^{-1}d^{-1}\mathbf{e}_x$. This force density was mainly uniform in regions where both the current and the magnetic fields were so, i.e., on the bulk of the magnets. However, it involved large gradients at the magnet boundaries where the magnetic field reverses direction. This gave rise there to large vorticity sources, $\Omega=\nabla\wedge\mathbf{f}\approx-(\mathbf{j}\cdot\nabla)\mathbf{B}$, which resulted in the generation of a chain of contrarotative electroconvective cells [Fig. 3(b)]. Their width, 12 mm or 6 mm, and depth, 3 mm, were set by the channel size but their length, 20 mm, was defined by the magnets.

B. Front observation and velocity measurement

The solution is observed from above with a charge-coupled device (CCD) camera involving 1046×768 pixels.

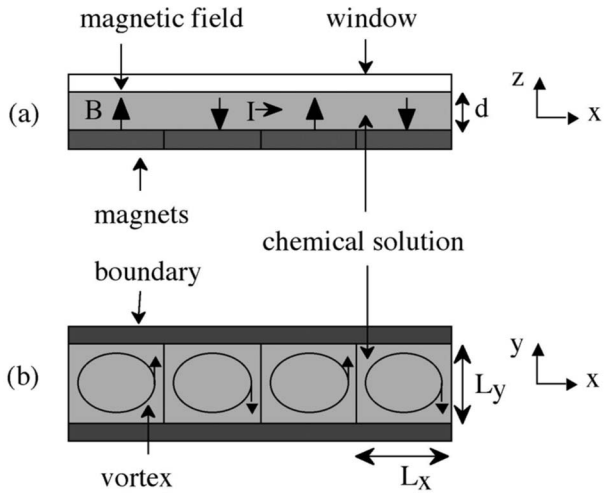

FIG. 3. Sketch of the experimental setup showing the fluid channel, 12 mm or 6 mm large and 3 mm thin, the magnets, 20 mm large, the magnetic field B, the electric current I, and the resulting electroconvective vortices. For the sake of clarity of the drawing, the fluid depth is enlarged and four vortices over ten in the actual chain are displayed. (a) Side view. (b) Top view. $L_x=20$ mm, $L_y=12$ or 6 mm, $d=3$ mm.

This provided a minimal accuracy of 0.2 mm by pixel when viewing the whole channel. Zooming on definite parts of the experiment enabled to increase it up to a factor 10. The front evolution was recorded on a MacIntosh computer. The front velocity being slow, a nominal sampling rate of 25 images per second was superfluous and memory consuming. A BTV Pro software has then been used to decrease this rate to one frame per second or below. In practice, the accuracy of velocity measurements were always dictated by spatial measurements rather than by time measurements. Owing to the inner scale displayed by fronts, e.g., the curvature radius of their tongues, the bound of accuracy came more from the difficulty in sharply localizing an event, e.g., the beginning of the contamination of a separatrix or of a vortex, than from the optical accuracy. The net accuracy in velocity measurements then varied from better than 0.1 mm mn^{-1} on effective propagation in the channel (Sec. IV B) to 1 mm mn^{-1} on the crossing of vortex separatrixes (Sec. IV D).

C. Hydrodynamical regime

To determine the hydrodynamical regime, the fluid depth d has to be compared to the nominal width ζ of the boundary layers at the top and bottom plates: $\zeta\approx\gamma(L_y\nu/2U)^{1/2}$, where $\nu\approx 1$ mm^2 s^{-1} denotes the water kinematic viscosity and where $\gamma=O(1)$ stands for the mean nondimensional slope of the velocity profile in the boundary layers (Appendix C). One then notices that, for flow velocities U below $U_{HS}=2\gamma^2L_y\nu/d^2$, boundary layers invade the whole cell depth: $\zeta\geqslant d/2$. The fluid is then in a Hele-Shaw regime that is suitable to exhibit planar flows. We shall keep in this regime in the whole experiment. As $\gamma\approx 1/2$ here, this corresponds to $U<U_{HS}=40$ mm mn^{-1} for $L_y=12$ mm and $U<U_{HS}=20$ mm mn^{-1} for $L_y=6$ mm.

When vortices experience upper or lower rigid bounds, secondary flows way result from the breaking of the balance between centrifugial force and pressure gradient in the boundary layer (Appendix C, Fig. 28). In particular, in a closed box involving a vortex, this is known to induce inward spiral trajectories and secondary vortices that are reminiscent of Eckman pumping [39–42]. However, although this mechanism is always at work, its intensity depends on the ratio of the cell depth d to the natural width ζ of the boundary layer. In particular, if d is too large compared to ζ, the secondary flow sources are restricted to boundary layers so narrow compared to the whole system that they negligibly put the whole fluid into supplementary motion: the intensity of secondary flows is then extremely small. On the opposite case of very narrow d compared to ζ, the secondary sources invade the whole medium. However, viscous effects are then dramatically large so that, even strong, these sources cannot give rise to noticeable flows. It is thus only for moderate cell depths of the order of ζ that secondary sources and viscous effects are respectively strong enough and small enough for yielding a relevant flow.

In practice, the ratio d/ζ beyond which secondary flows begin to be significant corresponds to boundary layers just coming into contact: $d/\zeta \approx 2$, i.e., to the limit of the Hele-Shaw regime. As our experiment remained in this regime, its vortex flows $\mathbf{V}$ could be considered as actually planar, $\mathbf{V}\cdot\mathbf{e}_z=0$.

In contrast with the boundary conditions assumed by theoretical models and simulations [17–20], the flow vanishes here at the channel boundaries. This, in particular, made the planar flow intensity vary on the depth direction. However, this gradient did not lead noticeable implications, presumably because the important phenomena were settled in the midplane where the flow intensity was the largest. Another implication of rigid boundaries was the vanishing of the flow at the lateral boundaries of the channel and the resulting velocity gradients in their vicinity (Fig. 27). We took them into account to finely analyze and model the effects of flow advection (Sec. VI).

D. Chemical reaction

Front propagation is produced by an autocatalytic reaction in aqueous solution, the chlorite-iodide reaction [43–50]. Its detailed mechanisms may be reduced into the following three equations reaction scheme [44,48]:

$$ClO_2^- + 4I^- + 4H^+ \rightarrow Cl^- + 2I_2 + 2H_2O, \quad (17)$$

$$5ClO_2^- + 2I_2 + 2H_2O \rightarrow 5Cl^- + 4IO_3^- + 4H^+, \quad (18)$$

$$IO_3^- + 5I^- + 6H^+ \rightarrow 3I_2 + 3H_2O. \quad (19)$$

Here, iodide I^- is oxydized in iodine I_2 (17) which in turn is reduced in iodate IO_3^- (18). As iodate also serves to oxydize iodide (19), the consumption of iodide is thus enhanced by one of its product, iodine: the reaction is in this sense autocatalytic. It is then usually studied in an excess of chlorite so as to focus attention on the nonlinear dynamics of iodide consumption. Depending on the level of homogeneity, through flow, and mixing in the medium, it is then known to provide bistability, oscillations, or waves [43–50].

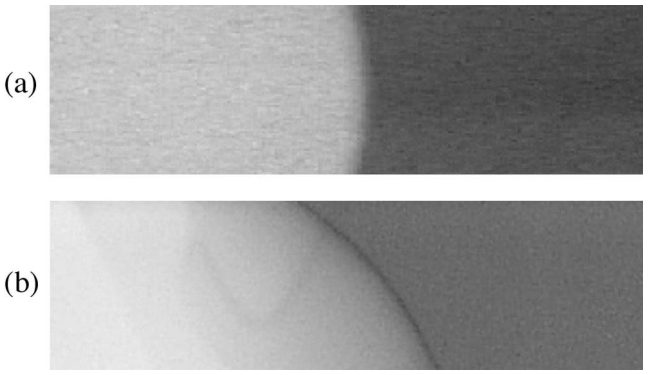

FIG. 4. Laminar front in a channel: the colorless wave propagates from left to right. (a) Top view of the front. Channel width and depth are 12 mm and 3 mm. (b) Side view of the front enlarged over a quarter depth. Channel depth is 10 mm.

Observation of a spatial wave is achieved by adding a starch indicator which, in the presence of iodide and iodine, gives rise to a blue starch-triiodide complex. Initially, the medium is thus colored due to this complex. However, as the wave passes through, the depletion in iodide and iodine leaves a colorless medium whose frontier with the blue medium localizes the front (Fig. 4).

In practice, we prepared sodium chlorite and potassium iodide solutions both at a concentration of 10^{-2} mole l^{-1}. These solutions were combined so as to yield the following species concentration, $[I^-]=3\times10^{-4}$ mole l^{-1}, $[ClO_2^-]=3.75\times10^{-4}$ mole l^{-1} and the pH was stabilized at 5 using a buffer solution. As the starch indicator was introduced, the solution took a blue color in about half an hour. This indicated that the reaction was uniformly proceeding in the medium, thereby slowly producing iodine I_2 and consuming iodide I^-. In absence of front initiation, this color could persist about an hour in a stirred medium until leaving a colorless fluid after total consumption of iodine. Meanwhile, the medium was thus in a weakly unstable state, $\theta \approx 0$, suitable for exhibiting a reaction-diffusion wave, provided a sharp concentration gradient was initiated somewhere.

Initiation of the reaction was achieved by contact of the solution with a piece of steel at one end of the channel. The resulting oxydation led a localized raise of iodine concentration following which the autocatalytic reaction speeded up. As a result, a colorless domain extended through the medium at the laminar front velocity V_o.

Transient effects prior to the establishment of a constant front velocity were weak enough to stand below our resolution. In particular, no variation of the front velocity could be noticed as reaction proceeded in the fluid at rest. However, some spontaneous initiations could randomly occur at the channel boundaries. They then gave rise to additional fronts that prevented the front under study to reach the channel end. Their occurrence was rare enough, however, for allowing the study of front propagation in the whole available space.

E. Front structure

Figure 4(a) shows a photograph taken from above of a laminar front propagating in a fluid at rest. It thus displays a picture of the front in the horizontal plane, the light intensity being integrated on the depth direction. We analyze in Fig. 5 this signal on the central line $y=L_y/2$ parallel to the largest side of the channel by plotting the normalized grey level intensity θ. As this line is normal to the front, the graph $\theta(x)$ enables us to access to the front inner structure. In particular, measurement of $\lambda=\theta'(M)^{-1}$ at the half-level point M where $\theta(M)=1/2$ yields a thickness $\lambda\approx 1$ mm. Although the level θ is related to the concentration of the complex starch triiodide instead of that of a single species, this determination of λ is quite representative of the distance over which a significant amount of reaction takes place, i.e., of the effective front thickness.

However, as the variable θ follows from optical integration over the channel depth d, it may result from a superposition of a range of thinner fronts slightly translated in direction x. This is confirmed by a side view of the laminar front in a deeper channel [Fig. 4(b)] which shows evidence of a thin front slightly curved on the depth direction. The origin of this curvature can hardly refer to thermics, as no noticeable raise of temperature due to the chemical reaction could be evidenced, but rather comes from the density differences between reactants and products which may induce an additional buoyancy-driven transport of species for large enough channel depth d [30–33]. This effect should reduce in more confined channels to finally become negligible below some depth value. This is corroborated here in Fig. 6 by the decrease of the effective front thickness λ with d until reaching a constant value for $d\leqslant 3$ mm and by the similar evolution of the front velocity V_o. Analyses of laminar fronts in Figs. 4(a) and 5 as well as the remaining of our study have then referred to this channel-depth-independent regime.

The front velocity V_o slightly varies with temperature at a rate of 0.2 mm mn^{-1} per degree. However, no significant raise of temperature was induced by the reaction and care has been taken to perform experiments at a fixed temperature of $T=19.5$ °C. Accordingly, the slight dependence of front velocity with temperature had no opportunity to operate, as confirmed by the steadiness of laminar fronts.

The order of magnitude of the front thickness $\lambda\approx 1$ mm is consistent with the KPP solution (2) and (3) for $V_o\approx 2$ mm mn^{-1} and $D\approx 2\times 10^{-9}$ m^2 s^{-1} according to which $\lambda=4f'(0)f(1/2)^{-1}D/V_o$. Whereas $f'(0)=1$, an estimate of $f(1/2)$ can be obtained by considering a parabolic form for $f(\cdot)$ satisfying $f(0)=f(1)=0$. One obtains $f(1/2)=1/4$ and $\lambda\approx 16D/V_o=0.96$ mm. The related reaction time τ then writes from Eq. (2) $\tau=4D/V_o^2\approx 7$ s.

The major cause of variation of front velocity was due to the electric current induced in the solution. This current modifies the ionic transport through the front and thus its inner dynamics and the resulting velocity. In particular, the resulting change of front velocity may be expected to depend on the respective directions of the electric current and of front propagation. This is confirmed in Fig. 7(a) where the observed velocity at $d=3$ mm is plotted as a function of current intensity I for a fixed direction of the electric current

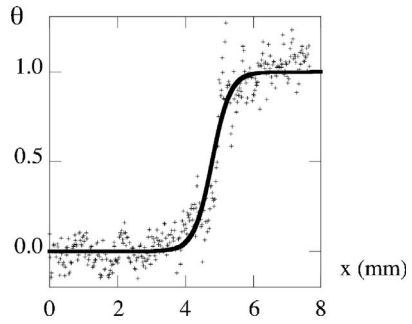

FIG. 5. Plot of the normalized grey levels θ of a front image along the central line $y=L_y/2$ of the channel. They correspond to the concentration of the starch-triiodide complex integrated on the cell depth and thus of the locations where a significant amount of reaction actually takes place.

$\mathbf{I}=I\mathbf{e}_x$ but for the same, $\mathbf{e}_x$, or the opposite, $-\mathbf{e}_x$, directions of front propagation. It is then found that front velocity is increased by the electric current, but four times more when the front propagates in the direction of the current.

F. Front local velocity

In the present Hele-Shaw regime, the actual flow $\mathbf{V}(x,y,z)$ involves a Poiseuille profile. Its variation in the depth direction then raises the question of the local velocity of a front part advected by this flow. The answer depends on the level of confinement measured by the Péclet number $\eta=dV_o/2D$ [29,51]. For low η, the normal front velocity corresponds to its laminar velocity plus the depth-averaged value of the flow $\mathbf{V}$ projected on the direction of propagation $\mathbf{n}$; for large η, it is the laminar velocity plus the maximal value $\mathbf{U}(x,y)$ of the flow $\mathbf{V}$ projected on the direction $\mathbf{n}$.

The value of η, 25 here, places the experiment in the wide gap regime where the local normal front velocity V_n writes

$$V_n = V_o + \mathbf{U}\cdot\mathbf{n}. \tag{20}$$

G. Flow intensity

The expected flow intensity U is weak enough, $U<35$ mm/mn, for keeping within the Hele-Shaw regime. This means that the nonlinear advection term remains negligible in the flow equation, so that raising the density of Laplace forces with the electric current density linearly increases the flow intensity while keeping its streamlines unchanged. This allows the maximal flow velocity to be chosen as a typical flow intensity representative of the whole flow intensity (Sec. II B).

To experimentally determine the maximal flow intensity U, we use the front as a suitable tracer for evidencing the quickest streamline at its first run from one separatrix to the other. The condition for this is that the front fully invades the whole boundary layer so as to ensure that it actually visits the quickest streamline. Then the gradient of flow intensity is expected to distort the front so as to provide evidence of the quickest streamline as the trajectory of the tip of the resulting front tongue (Fig. 8). The above condition bounds the flow

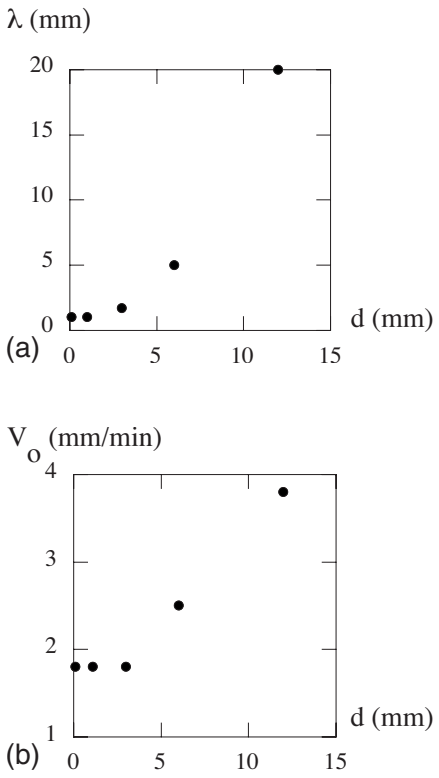

FIG. 6. Evolution of the thickness and the velocity of a laminar front with the solution depth d. (a) Laminar front thickness λ as seen from above the channel. (b) Laminar velocity V_o.

velocity to moderate values, $U/V_o<10$ [Figs. 8(a) and 8(b)], beyond which the front visits only a part of the boundary layer at its first rollup in a vortex [Fig. 8(c)].

In this moderate advection regime, the trajectory of the tip of the front tongue appears to be located near—but not at—the channel boundary and to display a nearly straight part parallel to the boundary [Figs. 1(a), 8(a), and 8(b)]. Flow velocity is then directed in average on the mean direction of propagation so that the resulting effective front velocity simply amounts to the sum of the flow intensity U and of the laminar velocity V_o. Removing V_o from the measured velocity thus provides a relevant measurement of U [Fig. 7(b)]. In particular, following the trajectory model developed in Sec. VI, the relative error in flow velocity made in assimilating the front tip to the most advected front point, i.e., the quickest trajectory $\tilde{r}'\approx 0.9$ to the quickest streamline $\tilde{\delta}'=0.78$ in Fig. 24(a), keeps smaller than 10% in the moderate advection regime: $U(\tilde{r}')/U(\tilde{\delta}')>0.9$ in Fig. 19.

The linear variation of the flow intensity U with the current intensity I is confirmed in Fig. 7(b) to a good accuracy. To minimize data scattering and extend data determination to larger flow intensities, we shall determine further on the maximal flow intensity U from its best linear fit to the current intensity I. This results in a constant relative error of 10% at most.

H. Eïkonal regime

In the present Hele-Shaw regime where the flow is planar (Sec. III A), it will be convenient to consider the propagation of the front in the plane located at middepth, where the flow amplitude is maximal. Then, in the present wide-gap regime (Sec. III F), each front part locally propagates in the local fluid frame with a normal velocity which, up to curvature corrections, is the laminar velocity V_o of a planar front. Propagation is then analogous to that of a phase front in the eïkonal approximation of optics, but in a steadily stirred medium here.

IV. EXPERIMENTAL RESULTS AND ANALYSES

We report below spatiotemporal features of fronts that are relevant to build a model of front propagation in a vortex chain. We first describe the sequence of events occurring during propagation and the resulting mean relative enhancement of front velocity. We then address the burning time of

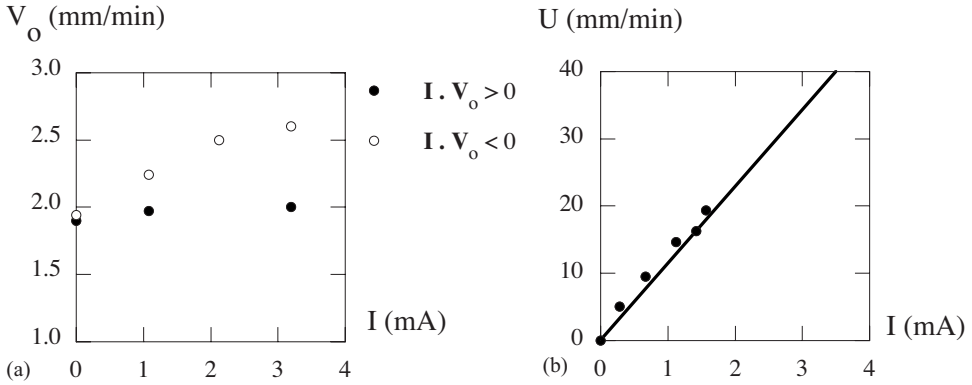

FIG. 7. Evolution of the laminar velocity and of the flow intensity with the current intensity. (a) Laminar velocity V_o: full (respectively, open) points refer to a front propagating in the same direction as the electric current, $\mathbf{I}.\mathbf{V}_o>0$ (respectively, in a direction opposite to the electric current, $\mathbf{I}.\mathbf{V}_o<0$). (b) Flow intensity U. Measurements are performed in the moderate velocity regime on the front parts that are the most advected close to the channel boundary. They correspond to the tips of the tongues displayed by the front in the boundary layers [Figs. 8(a) and 8(b)]. The flow intensity is obtained by removing the laminar front velocity from their velocity. It evolves linearly with the current intensity I.

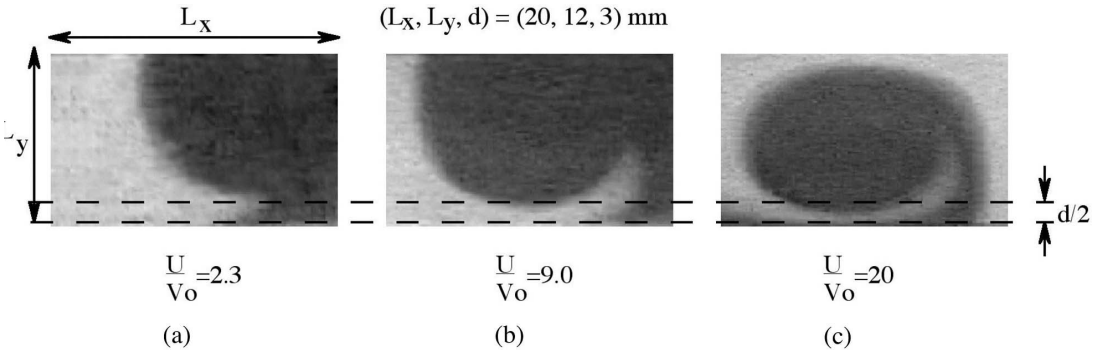

FIG. 8. Front images evidencing the flow boundary layer at various flow intensities: (a) $U/V_o=2.3$, (b) $U/V_o=9$, (c) $U/V_o=20$. In all cases, boundary layer thickness is about half the cell depth.

vortices and sepatrices, the length of front wakes and the thickness of flow boundary layers.

Unless explicitly stated, the experimental results will refer to the 12 mm channel width. However, interesting variations with the channel width will also be evidenced.

A. Qualitative features of front propagation

Observations and measurements have referred to fronts initiated at the extremities of the vortex chain and in a steady flow. Quickly after initiation, the front invades the whole channel section. It is then rolled up by vortices but succeeds in maintaining a sharp transition between the blue fresh medium and the colorless burnt medium (Figs. 1, 14, 10, and 11), as expected in the flamelet regime.

At large flow velocity compared to the laminar velocity, several cells burn simultaneously. The front is then extended on a wake that spreads from just contaminated cells to nearly fully burnt cells (Figs. 1 and 14). Interestingly, the front is closed on itself in each cell and proceeds from the cell periphery that is fully burnt to the cell center that is fully fresh. Viewed from the whole wake, it is therefore *disconnected* and exhibits independent dynamics from one cell to the other. In particular, as the disconnected parts of the front are separated by fully burnt zones where the species concentration gradient vanish, no diffusion flux can couple them. Moreover, as they belong to different cells, no advection flux can connect them either. They thus behave *independently* one from the other.

When contaminating a vortex cell, the front is first advected on efficient streamlines located near the channel boundaries (Figs. 1, 14, 8, and 15). They are however distant from them by a short, but significant distance (Figs. 8 and 15). The front then reaches the vortex separatrix, the other channel boundary and the second vortex separatrix. This makes it close on itself leaving a connected slightly elliptical front advancing towards the vortex center until disappearing (Figs. 10 and 11). Meanwhile, the part of front left close to the vortex separatrix enters the neighbor vortex and is advected towards the channel boundary. The same scenario as above then resumes, giving rise to a periodic propagation through the vortex chain with possibly several contaminated vortices at a time (Figs. 1 and 14).

Interestingly, the fine shape of the whole front depends on the reduced flow intensity U/V_o, i.e., on the relative magnitude of advection compared to propagation. This is apparent in Fig. 1 where, at similar phases of propagation, the front penetration in vortices appears larger at a low reduced velocity ($U/V_o=9.0$) than at a twice larger value ($U/V_o=18.8$). Similar observations can be made on Figs. 14, 8, 11, and 15 with noticeable implications regarding the length of a front wake (Figs. 1 and 14).

Careful examination of the advected tongues shows that the colorless zone left behind the front looks slightly less bright than on other front parts and its transition to the dark zone slightly less sharp (Fig. 1). This must not be interpreted as an evidence of a thick front, but instead as a result of the optical integration over the cell depth, similar to that discussed on laminar fronts (Sec. III E). In particular, as the front is present only on a part of the fluid depth there (the middle part), the integrated intensity lies in between bright and dark on these specific zones. This is consistent with the existence of a planar flow involving a varying intensity on the cell depth, as expected in the present Hele-Shaw regime (Sec. III A). On the foremost parts of the front, this gradient then yields a differential advection which is responsible for a partial occupation of the channel depth. However, further propagation of the front to the top and bottom boundaries makes it invade the whole channel in the wake, yielding a sharper transition as seen from above.

B. Relative enhancement of front velocity

The effective velocity V_f of the front has been measured as the mean velocity of its foremost point on the mean direction of propagation $\mathbf{e}_x$ and on the longest relevant front path. As fronts reached a constant mean velocity since the first contaminated vortex, this path actually extended over the whole ten vortex chain. With an absolute uncertainty of 1 mm and 1 s on length and time and a maximum effective velocity of 15 mm mn^{-1}, this provided a relative uncertainty $\delta V_f/V_f$ less than 7×10^{-3}.

The relationship $V_f/V_o=\Psi(U/V_o)$ between the nondimensional effective velocity V_f/V_o and the nondimensional flow intensity U/V_o is displayed in Fig. 9 for the two channel widths $L_y=12$ mm [Fig. 9(a)] and $L_y=6$ mm [Fig. 9(b)]. In each of them, cellular flow is found to enhance the effective

front velocity, in agreement with the additional transport property brought about by advection: $\Psi'(\cdot)>0$. However, this effect is found to weaken as the flow intensity is increased: $\Psi''(\cdot)<0$. This is noticeable for the 12 mm width since the slope of the function $\Psi(\cdot)$ is found to decrease from 0.6 for $U/V_o<3$ to 0.12 for $13<U/V_o<20$, i.e., by a factor 5 on the observed range [Fig. 9(a)]. For the 6 mm width, the smallest bound of the Hele-Shaw regime does not allow this efficiency damping to be apparent until the largest data point of the experimental range [Fig. 9(b)].

On the other hand, an important feature brought about by the comparison between Figs. 9(a) and 9(b) is the dependence of the velocity enhancement V_f/V_o on the channel width L_y: the larger the channel width, the larger the velocity enhancement. This, in particular, means that there is no universal relationship independent of the channel geometry here. This contrasts with the picture brought about by renormalization approaches [17–19]. This also indicates that boundary effects and thus the vortex structure play a significant role that needs to be taken into account in modeling.

C. Vortex burning time

In the front wake (Figs. 1 and 14), images display elliptical fronts that reduce in time until vanishing. As these connected fronts are tangent to the flow streamlines, their propagation is not enhanced by advection. It thus only results from reaction-diffusion. To test this statement, we have measured the velocity of these fronts, care being taken of the direction of propagation $\mathbf{n}$ with respect to that of the electric current density $\mathbf{j}$. In particular, whereas a modification of front velocity V_o is observed for front propagation parallel to current $\mathbf{j}$, no effect is expected for front propagating normal to it. This is confirmed on a large range of current in Fig. 12 where the reduction speed of the ellipse axis parallel to the channel width, i.e., satisfying $\mathbf{j}\cdot\mathbf{n}=0$, is found to be consistent with the nominal laminar velocity V_o previously measured in the $\mathbf{e}_x$ direction in absence of current ($\mathbf{j}\cdot\mathbf{n}=0$). On the other hand, measurements of front velocity on the middle axis $y=L_y/2$ of the channel agree with the laminar velocity found for fronts moving in the direction of the current ($\mathbf{j}\cdot\mathbf{n}>0$) or in the counterdirection ($\mathbf{j}\cdot\mathbf{n}<0$).

The burning of a vortex appears to involve two phases:

(1) A quick contamination of the inner vortex separatrix in a vortex turnover time. This phase lasts a time of about $t_1=2(L_x+L_y)/U$ and ends up with a closed elliptical front.

(2) the vanishing of the elliptical front. Since, at the end of the first phase, the initial distance $L_y/2$ to the vortex center is reduced by the distance $V_o t_1$ yet crossed by the front, this phase lasts a time of about $t_2=(L_y/2-V_o t_1)/V_o=L_y/2V_o-t_1$.

The total vortex burning time $T_b=t_1+t_2$ thus reads $T_b\approx 1/2\ L_y/V_o$. It means that each vortex burns at the laminar velocity, independently of the flow intensity. This is confirmed in Fig. 11 where the burning of a vortex is achieved at two flow intensities: although advection and front shape differ, the vortex burning time is the same.

D. Separatrix burning time

Advance of the front along its mean direction of propagation is found to slow down at the vortex separatrix. This indicates a difficulty in contaminating neighbor vortices which eventually penalizes the net efficiency of front propagation. To quantify this effect, we have measured the mean velocity V_s of the front on the x axis during propagation from the outer border of the elliptic front formed in the cell to the entry in the neighboring cell.

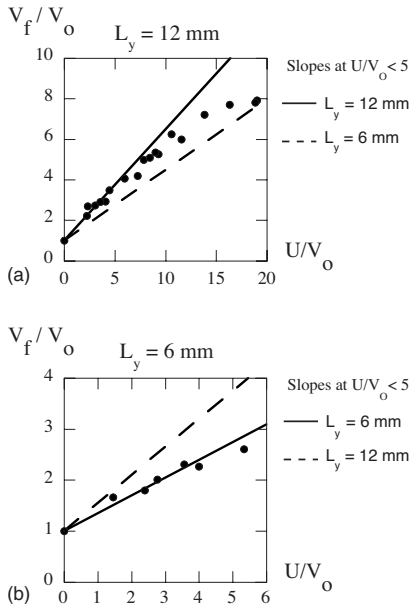

FIG. 9. Effective front speed V_f in cellular flow in the Hele-Shaw regime as a function of U in the units of the laminar velocity V_o. Vortex sizes (L_x, L_y) are (20,12) mm in (a) and (20,6) mm in (b) and the channel depth is 3 mm. The loose of efficiency of velocity enhancement by vortex flow is noticable in (a). In the more confined channel (b) in which the Hele-Shaw regime is twice more restricted, it is however only weakly apparent at the largest data point. The slopes at low velocity amplitude ($U/V_o<5$) are 0.55 for L_y=12mm and 0.37 for L_y=6mm. They are shown by full lines (resp. dotted) lines corresponding to the actual (resp. other) vortex width. The differences with vortex aspect ratios show the relevance of sub-scales in the effective front velocity and the need for more than one-scale modeling.

Figure 13 reports the nondimensional velocities V_s/V_o and $(V_s-V_o)/V_f$ for various relative flow velocities U/V_o. It is found that, whatever the flow velocity, the effective velocity V_s across a separatrix is significantly lower than the effective velocity V_f and equals to about the laminar velocity V_o, up to experimental uncertainty: $V_s\approx V_o$. In particular, whereas the relative uncertainty is large on V_s/V_o, it is small on $(V_s-V_o)/V_f$. Accordingly, seen at the scale of the front velocity V_f, V_s cannot actually be distinguished from V_o. This means that separatrixes are crossed by reaction-diffusion only.

E. Front wake

While the front advances at velocity V_f in the vortex chain, the contaminated cells left behind continue to burn. They then give rise to a wake extended on a number N of incompletely burnt vortices. Given the total vortex burning time T_b, this number reads $N=V_f T_b/L_x\approx 1/2\ L_y/L_x\ V_f/V_o$. In

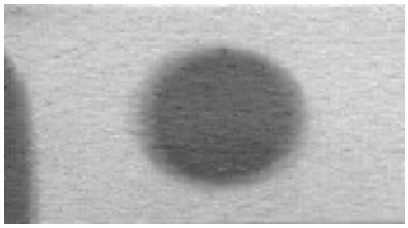

FIG. 10. Elliptical shape of a closed front inside a vortex.

particular, for the 12 mm channel width, this gives $L_x/L_y = 5/3$ and $N=3/10\ V_f/V_o$.

Figure 14 shows three images taken at the same phase of the cycle and for which the predicted values of N are 0.9, 1.6, 2.35. Accordingly, one thus expects a wake extended on about a vortex, a vortex and a half, and two vortices and a half. The qualitative agreement with the images of Fig. 14 validates this kinematic determination of the wake structure.

F. Thickness of the flow boundary layer

Following the velocity gradient of the vortex flow, the front experiences a differential advection which imprints its geometry. This in particular gives rise to tongues from which one may guess inferring the main structure of the flow. This inverse problem requires decoupling the respective contributions of the proper front velocity V_o and of the flow field $\mathbf{U}$ to the front evolution so as to infer the location of the fastest streamline of the flow. This analysis is conditioned by the relative flow intensity U/V_o.

At large flow intensity compared to laminar front velocity, e.g., $U/V_o \approx 20$ [Figs. 14(c) and 8(b)], front advection in a vortex is so large that the proper front propagation can be neglected there. The front then behaves as a passive tracer whose differential advection evidences the flow velocity gradient. However, as the front enters the vortex boundary layer from its outer frontier with a neighbor vortex, contamination of the whole boundary layer requires propagation normal to the flow streamlines. As this is much less efficient than advection here, the fastest streamline is unlikely reached over a vortex turnover. Accordingly, the tongue thickness observed near the boundary only bounds the boundary layer thickness by *below* [Fig. 8(c)]. At the opposite limit of weak flow intensity, e.g., $U/V_o=2.3$ [Fig. 8(a)], the advection of the front is sufficiently slow for allowing it to invade the whole boundary layer before it arrives at the channel boundary. Then, the tongue tip evidences the fastest streamline but the tongue thickness goes over the boundary layer thickness. Finally, for flow intensity in between, e.g., $U/V_o=9.0$ [Fig. 8(b)], the tongue tip still fits into the boundary layer while the tongue thickness gives about the boundary layer thickness.

Figure 8 displays the tongues observed in these three cases near the channel boundary. They provide the following estimations for the boundary layer thickness Δ: $\Delta < 1.8$ mm [$U/V_o=2.3$, Fig. 8(a)], $\Delta \approx 1.5$ mm [$U/V_o=9.0$, Fig. 8(b)], $\Delta > 0.9$ mm [$U/V_o=20$, Fig. 8(c)]. This points to a boundary layer thickness of about half the cell depth: $\Delta \approx d/2 = 1.5$ mm. Introducing the distance $\delta = L_y/2 - \Delta$ of the boundary layer to the cell center and its relative value $\delta' = \delta/(L_y/2)$ compared to the available distance $L_y/2$, these estimations yield the following bounds: $4.2 < \delta < 5.1$ mm and $0.70 < \delta' < 0.85$.

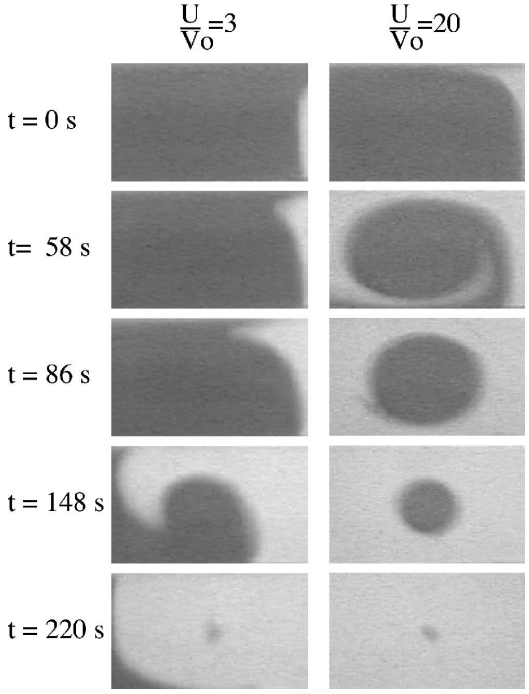

FIG. 11. Front propagation in a vortex. Comparison between two relative flow intensities, $U/V_o=3$ and $U/V_o=20$, at the same laminar flow velocity $V_o=1.9$ mm mn^{-1} and the same vortex size $(L_x,L_y)=(20,12)$ mm. In both cases, the vortex burning time T_b is the same, about the predicted time $1/2\ L_y/V_o=189$ s.

In the present Hele-Shaw regime, viscous dissipation is handled by boundary layers at the horizontal plates. It then enables the averaged flow to accomodate the lateral boundary conditions over a distance of half the cell depth, independently of the flow intensity (Appendix C, Fig. 27). This property agrees with the above determination of the boundary layer thickness.

In the following, we shall develop a model based on vortices involving equal widths and lengths. To corroborate the above determination of the boundary layer thickness in this case, we have performed the same study as above in a $15 \times 15 \times 3$ mm square cell. At weak advection ($U/V_o=1.6$, Fig. 15), the front tip indicates the location of the fastest streamline. This gives a boundary layer thickness about half the cell depth, in agreement with the present Hele-Shaw regime.

V. FRONT PROPAGATION MODELING

Measurements of the effective front velocity V_f in the range $0 \leqslant U/V_o < 20$ have revealed a reduction of the efficiency of velocity enhancement by advection: $\Psi''(\cdot) < 0$ where $V_f/V_o = \Psi(U/U_0)$ (Fig. 9). This nonlinearity cannot be attributed to a change of hydrodynamical regime since the fluid remained in the Hele-Shaw regime. It must then be

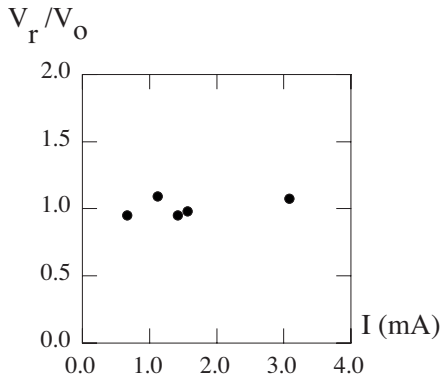

FIG. 12. Dynamics of an elliptical front. Comparison between the velocity of the front on the y-axis normal to the electrical current $\mathbf{j}$ and the laminar velocity V_o in absence of current: both are equal to the experimental uncertainties.

traced back to the interplay between propagation and advection.

As reported in Sec. II, a number of questions remain regarding this interplay and the nature of a relevant modeling of front propagation in the present flamelet regime. In particular, whereas the different models proposed to date [17–21] yield predictions that may be in quantitative agreements with some numerical observations, they refer to different, if not physically incompatible, foundations. On the other hand, previous experiments [28,37,38] are not sufficiently complete to provide accurate tests of models or suitable grounds to develop modeling. Therefore, our objective will be to question the nature of the effective front propagation observed in our experiment and identify the foundation of a suitable model to be worked out in the next sections.

A. Alternatives raised by the nature of front propagation

Although the local structure of the front remains the same in a medium at rest or in a vortex chain, its nature and its

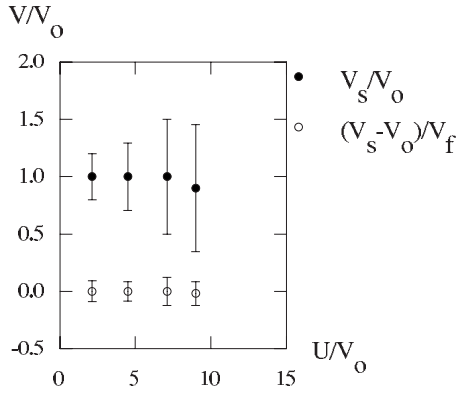

FIG. 13. Effective velocity V_s across a separatrix for different relative flow velocities U/V_o. The relative front velocities V_s/V_o and $(V_s-V_o)/V_f$ show that, to the accuracy of the measurements and seen at the scale of the front velocity V_f, V_s is confused with V_o. This means that separatrices can be considered as crossed by reaction-diffusion only.

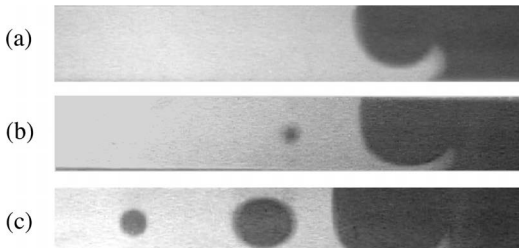

FIG. 14. Wake of the front for three different flow intensities. The predicted number of vortices in the wake is $N=3/10\ V_f/U_o$. Snapshots have been taken at the same phase of the rolling up of vortices so as to allow a direct comparison of the wakes. (a) $U/V_o=3.5$, $V_f/V_o=2.9$, $N=0.9$. (b) $U/V_o=9.0$, $V_f/V_o=5.4$, $N=1.6$. (c) $U/V_o=19$, $V_f/V_o=7.8$, $N=2.35$. In agreement with the expected values of N, a vortex (a), a vortex and a half (b), and two vortices and a half (c) are noticed on the wakes.

propagation mechanism may change when considered at a large scale. The reason for this traces back to the fact that averaging waves, spatially or temporally, may yield phenomena of a seemingly different nature. This is well-known regarding the wave/particle duality since wave interferences may yield a particle dynamics revealed by steepest descent method, stationary phase approximation, or extremalization of an action. Also, in heterogeneous media, wave interactions are known to possibly induce localization.

These famous examples warn us about the subtlety in determining the nature of the averaged front propagation and, therefore, in building a relevant model for it. To clarify this issue, we consider the mean concentration profile $\langle\theta\rangle(x,t)$ obtained by filtering out the vortex scale L_x and below from the field $\theta(x,y,t)$. Beyond transient, it is expected to behave as a traveling wave with velocity V_f: $\langle\theta\rangle(x,t)=\langle\theta\rangle(x-V_ft)$. Interestingly, three different alternatives arise regarding its nature.

A first alternative consists in stating whether the averaged profile refers to a wave, in the sense that all neighbor points interact, or to the wake of a propagating particle, in the sense that they do not, except at some leading points. An example of the wave case is given by hydrodynamic surface waves since neighbor points are *coupled* by the fluid motion beneath the surface. An example of the particle case is provided by the propagation of a fall in a domino chain. Here, dominos evolve by their own *independently* of their neighbors (except at the very time they are pushed down) but nevertheless collectively give rise to a propagating wake that resembles a wave profile. Therefore, in the wave case, the mean burning rate at a point should thus depend not only on its proper state *but also* on those of its neighbors; in contrast, in the particle case, this rate would only depend on the state of the point that is considered, *independently* of its neighbors, except at a definite leading point: the foremost point of the profile where contamination proceeds. Beyond the apparent similitude between propagating disturbances in these two cases, the different nature of their underlying couplings yields a large difference on their modeling and on the way their velocity is fixed: locally at the leading point in the particle case, nonlocally as a global equilibrium in the wave case. In particular, here, we stress that a field model is suit-

able to deal with reality on waves whereas it can at most mimick it on wakes.

A second alternative refers to the role of scales in modeling, especially those played by the vortex scale L and below. In particular, the fact that the scale L is filtered out from the mean front profile does not prevent it from playing a significant role in the determination of the mean front velocity. Is this implicit coupling then restricted to the sole vortex scale L or does it also extend to the subscales that characterize the fine structure of the vortex flow? The answer determines the level of subscale modeling required to determine the large scale features of the front. In particular, it will decide here whether the nature of the boundary conditions are negligible or essential regarding the effective front propagation.

A third alternative refers to the selection of the traveling wave solution $\langle\theta\rangle(x-V_f t)$: is it a unique solution or a solution selected among a continuum?; does selection then operate on specific locations of the actual profile and which ones? Notice that these questions already pertain to the laminar regime, since a KPP solution is selected among a continuum of solutions by the structure of the leading edge of the profile $\theta\approx 0$ (pulled front) whereas other kinds of production rate yield the selected solution to be monitored still by a definite zone of the profile but at a finite value of θ (pushed front) (Sec. II A).

The models based on renormalization [17–19] have answered these alternatives this way (Sec. II C). The mean propagating front follows an effective reaction-diffusion dynamics. It thus corresponds to an effective reaction-diffusion *wave* for which all points are *coupled* to their neighbors by diffusion. *Only* the vortex scale L enters the renormalized equation through coefficients that renormalize the diffusion coefficient D or the reaction time τ at a power of the Péclet number $\mathrm{Pe}=UL/D$. In particular, *no* dependence to the fine structure of the flow, and thus to its boundary conditions, is in order. In this framework, the mean front velocity then stands as a nonlinear eigenvalue of the dynamical equation: as for the laminar front, it should thus correspond to a *selection* among a continuum of eigenvalues whose nature depends on the nonlinear features of the renormalized reaction rate.

On the opposite, our experiment has revealed that, in the regime studied, cells of the wake are *not interacting* since they are burning from a periphery on which the value $\theta=1$ is uniformly reached (Fig. 1). In particular, the fact that the uniform bright state $\theta=1$, $\nabla\theta=0$, extends over a volume that encloses the dark connected zones $\theta=0$ that remain to burn (Fig. 1) implies the absence of concentration flux between the latter zones. As there is no advective flux between them either, the zones to burn are thus *decoupled* one from the other. Their burning time is then set by both their own state and the laminar velocity V_o, *independently* of the state of the neighboring cells. In particular, the effective front velocity is thus set not in the wake but *at* the foremost vortex cell of the front by the ability of the foremost point of the front to contaminate the neighboring cell.

This statement stresses that modeling front propagation in the present large Damköhler number regime cannot be obtained by effective coarse-grained equations from which the mean front velocity and the mean front profile would follow as selected eigenvalues and selected eigenvectors. Instead, attention has to be focused on the local events that occur at the foremost cell where contamination actually proceeds.

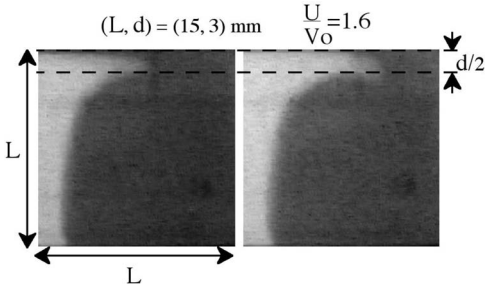

FIG. 15. Front propagation in a square cell of width $L=1.5$ cm and depth $d=3$ mm at $U/V_o=1.6$. Advection is weak enough for allowing the front to contaminate the whole boundary layer before arriving at the cell boundary. Its tongue tip then nearly corresponds to the fastest streamline. This evidences the boundary layer thickness at about half the cell depth and the relative distance of the fastest streamline to the vortex center, δ', in the range $0.70<\delta'<0.85$.

This difference with the modeling applied at small Damköhler numbers is presumably related to the level of fluctuations of the actual front with respect to its mean profile. After having addressed this below, we analyze the contamination process from cell to cell and we conclude about the nature of the modeling that could be appropriate to the present regime.

1. Scales and fluctuations

Observation of front propagation reveals three kinds of scales (Fig. 16):

(i) A global scale $L_g=N\,L_x$: it corresponds to the front wake and states the distance over which a front is displayed in the channel.

(ii) A local scale $L_l=L_x$: it corresponds to the vortex scale which imprints the global front structure.

(iii) Subscales $L_s<L_x$: they correspond to the fine structures of the front inside a cell, for instance the front tongues.

The level of fluctuations at scale L_x can be evaluated by comparing the y-averaged profile $\bar{\theta}(x,t)$ of $\theta(x,y,t)$ to the traveling wave profile $\langle\theta\rangle(x,t)$ at scale L_g obtained for instance by performing a gliding average over a period $(L_x, T=L_x/V_f)$ (Appendix B). For a small fluctuation level, subscales may be thought to be weak enough for playing no important role in the dynamics of the coarse-grained front. This is the assumption underlying the renormalization procedures [17–19] which actually concluded that the effective front satisfies a renormalized reaction-diffusion equation involving the sole scale $L\equiv L_x$ through the Péclet number $\mathrm{Pe}=UL/D$. On the opposite, for a large fluctuation level, subscale fluctuations display an order of magnitude similar to that of the coarse-grained front. One may then expect them to significantly influence both the coarse-grained profile $\langle\theta\rangle(x,t)$ and the mean velocity V_f.

Figure 17 reports three examples of propagating fronts with, for each, the profiles $\bar{\theta}(x,t)$ and $\hat{\theta}(x,t)$ of the

y-averaged field and of the corresponding traveling wave. The first two examples refer to fronts propagating in the vortex chain for $U/V_o=3.0$ and 13.8. The third one corresponds to a diffusive profile of a passive tracer observed in the same vortex chain. It then appears that the fluctuation rate is large in the propagating case [Figs. 17(a) and 17(b)] and weak in the diffusive case [Fig. 17(c)]. This corroborates the relevance of an effective diffusion equation to represent the diffusion of a passive tracer in a convective roll chain [13,14], but lays doubt on the validity of an effective reaction-diffusion equation [17–19] for modeling front propagation in the present large Damköhler regime.

2. Contamination process of cells

To address the mechanism of vortex contamination by the front, it is worth comparing the relevant length scales of the different transport processes that occur during advection along the vortex separatrix.

Advection along the separatrix from one channel boundary to the other typically lasts a time L_y/U. Meanwhile, diffusion spreads the front on a length $l_{diff}\approx\sqrt{DL_y/U}$. Compared to the front thickness $\lambda\approx\sqrt{D\tau}$, this diffusion length appears $l_{diff}/\lambda\approx\sqrt{\mathrm{Da}}$ larger. In our regime, $5<\mathrm{Da}<60$, this makes it of the same order of magnitude than λ, so that one cannot make a distinction between a pure diffusion zone and a reaction-diffusion zone during this advective phase. This statement contrasts with the strong advection regime $\mathrm{Da}\ll 1$, $l_{diff}\ll\lambda$, in which the sole diffusion is more efficient than reaction-diffusion to cross a separatrix [17–19].

Similarly, the propagation length during advection along a separatrix, $l_{prop}\approx V_oL_y/U\approx\sqrt{D/\tau}L_y/U$ also appears here about the diffusion length l_{diff} since $l_{prop}/l_{diff}\approx\sqrt{\mathrm{Da}}$. This corroborates the above conclusion following which reaction and diffusion are intricated during the contamination of a separatrix.

Following these analyses, the front therefore crosses the separatrixes by a coupled reaction-diffusion mechanism with no benefice from advection, i.e., by propagation at the laminar velocity V_o. This recovers the conclusion of the experiment analysis (Sec. IV D).

3. Basis for a model of effective front propagation

Observations stress a distinction between a foremost zone in which the front contaminates an additional vortex and a wake within which yet contaminated vortices finish to burn (Fig. 1). The important thing is that the former zone sets the effective velocity of the front by a specific mechanism, the crossing of a vortex separatrix, which is no longer at work in the latter zone where all separatrixes are already burnt. Although the periodicity of the global phenomenon yields all zones to evolve at the *same period*, the mechanisms that fix the actual value of the effective front velocity, and thus of the actual period, are thus to be sought in the detailed propagation of the *most advanced* part of the front. In turn, the effective front velocity sets the number of burning vortices and thus the structure of the front wake (Sec. IV E).

These remarks make the difference between the present front propagation and an effective reaction-diffusion wave.

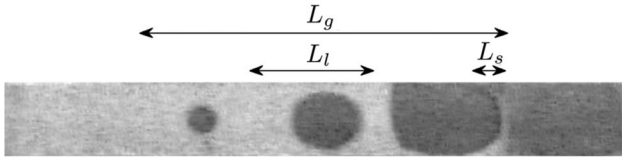

FIG. 16. Sketch of the different characteristic scales displayed on a front: a global scale L_g extending over the front wake, a local scale L_l equal to the cellular scale L_x, and subscales L_s corresponding to the fine structures shown by the front.

In particular, the existence of *two* independent relevant scales, the local scale $L_l=L$ at which the actual velocity is set on the foremost part of the front and the global scale L_g on which the wake extends, means that effective front propagation refers to *more* than a single scale function. This feature is confirmed in Fig. 9 by the dependence of front velocity on the vortex aspect ratio. It forbids the effective front propagation to be the solution of a differential equation involving a *single* characteristic length scale l_c. This especially includes reaction-diffusion equations, possibly renormalized, which actually exhibit a single scale: $l_c=(D\tau)^{1/2}$.

It thus appears that, in the present two-scales propagation phenomenon, advection effects cannot be reduced to a renormalization of effective coefficients of the laminar reaction-diffusion equation. As a consequence, the effective front velocity cannot be sought as the eigenvalue of a homogenous differential system or as the result of a global mechanism. Instead, it appears to be set in a bounded active region, the foremost part of the front, to be modeled at a *small scale* modeling. The following kinematic models are intended to recover its main features.

B. One-trajectory models

A kinematic model of front propagation in the large Damköhler regime has been introduced by Abel *et al.* [19] and Cencini *et al.* [21]. The cellular flow, modeled by the stream function (7), is two dimensional and undergoes free boundary conditions. The front is considered to propagate along the bottom boundary to the vortex separatrix, then move in its vicinity up to the top boundary and cross it to enter the next vortex. The same kind of motion then resumes.

The objective of these authors consisted in determining the kinematics on the mean direction of propagation $\mathbf{e}_x$ and thus in reducing the two-dimensional problem to a one-dimensional kinematics. For this, the component of the front velocity on direction $\mathbf{e}_x$ has been taken as the sum of the laminar front velocity V_o and of the flow component $\mathbf{U}\cdot\mathbf{e}_x=U\cos(\pi y/L)\sin(\pi x/L)$. Here, the ordinate $y(t)$ of the front position handles the two dimensionality of the issue. It is nearly constant when the front stands close to the $y=0$ or $y=L$ separatrix but changes value from 0 to L when it propagates from one to the other. It then appeared convenient to consider the time-average β of the factor $\cos(\pi y/L)$ on a trajectory:

$$\beta=\frac{1}{T}\int_0^T\left|\cos\left(\frac{\pi y(t)}{L}\right)\right|dt. \tag{21}$$

This provided the kinematic equation on the x axis:

$$\frac{dx}{dt} = V_o + \beta U \left| \sin\left(\frac{\pi x}{L}\right) \right| - \left[\beta - \left| \cos\left(\frac{\pi y(t)}{L}\right) \right| \right] U \left| \sin\left(\frac{\pi x}{L}\right) \right|. \quad (22)$$

Neglecting the last term of Eq. (22) then yields a one-dimensional equation for front propagation [19,21]:

$$\frac{dx}{dt} = V_o + \beta U \left| \sin\left(\frac{\pi x}{L}\right) \right| \quad (23)$$

where the prefactor β accounts for the mean effect of the variation of front position on the y axis.

As β depends on the trajectory, it *a priori* changes with the reduced flow velocity U/V_o. In particular, β would be strictly unity if the trajectory was along the separatrix $y=0$ or $y=L$, but is actually less since front trajectories stand within the vortices. However, assuming a weak dependence of β on U/V_o, integration of Eq. (23) with constant β yields relation (16). This corresponds to fixing the trajectory and thus working within a one-trajectory model.

In Refs. [19,21], β was not determined from modeling but from numerical simulations at definite values of U/V_o: $\beta \approx 0.89$ [19] or $\beta \approx 0.875$ [21]. This provided in both cases a good agreement between relation (16) and numerical simulations. The difference between β and unity reflects both the distance of the front trajectory to the $y=0$ or $y=L$ separatrix and the time spent in going from one separatrix to the other.

A particular case has been considered by Vladimirova *et al.* with a front strictly following separatrixes [20]. Here, the front used the separatrixes parallel to y to alternate between those located at $y=0$ or $y=L$ while advancing on the x direction. Then, on each straight part of this trajectory, either parallel to the x or y directions, the kinematics is given by Eq. (23) with β strictly equal to unity, so that the mean front velocity satisfies relation (16) with $\beta=1$. In particular, the time spent on each of them is the same, whatever their direction. However, the path followed on the front trajectory is twice as long than its projection on the x axis. Accordingly, the predicted effective front velocity on this axis is only *half* the velocity given by relation (16) for $\beta=1$. This prediction appears to strongly disagree with numerical results to about a factor of 2. This indicates that the advance of the front on the x axis during the propagation from one separatrix (e.g., $y=0$) to the other (e.g., $y=L$) stands as an essential feature of the issue.

These results emphasize the sensitivity of the effective front velocity to the front trajectory and thus, to the flow boundary conditions. This in particular forbids a relevant comparison between the present experimental data (that are obtained on *rigid* boundary conditions) and relation (16) (that is derived for *free* boundary conditions). On a deeper ground, this calls for a model capable of accurately determining the path followed by the front and its implication on the effective front velocity V_f.

C. Multitrajectory model

Following the above analysis, we thus propose to build a local kinematic model for front propagation capable of handling the sensitivity of front velocity to trajectories.

We thus consider the most advanced point M of the front in the mean direction of propagation $\mathbf{e}_x$ and assume that, in the large Damköhler regime, its kinematics satisfies the eïkonal approximation (20) (Sec. III F). Its normal velocity then reads: $\mathbf{V}_M \cdot \mathbf{n} = V_p + \mathbf{U} \cdot \mathbf{n}$ where V_p denotes the proper normal front velocity with respect to the medium. Restricting attention to a large relative vortex size ξ, we shall consider, in agreement with observations, that the front curvature in M is large compared to the front thickness. Then the proper velocity V_p reduces to the laminar velocity V_o of a planar front so that

$$\mathbf{V}_M \cdot \mathbf{n} = V_o + \mathbf{U} \cdot \mathbf{n}. \quad (24)$$

In contrast with previous models, we do not seek to prescribe a definite trajectory for the front. Instead, we take advantage of experimental observations to qualitatively model its geometrical features, leaving free the corresponding geometrical parameters p. We obtain this way a one-parameter family of trajectories $\mathcal{T}(p)$ among which we shall let a dynamical selection operate.

The selection path will naturally correspond to the fastest one. This is legitimated by the fact that only the fastest path can survive the dynamical competition among paths, the fate of slower paths being to be eventually overwhelmed by front propagation on the fastest path.

Calling $T(p)$ the transit time of the foremost point M in a vortex, the selected trajectory $\mathcal{T}(\tilde{p})$ will thus obey a least-time criterion:

$$\frac{dT}{dp}(\tilde{p}) = 0; \quad \frac{d^2T}{dp^2}(\tilde{p}) > 0. \quad (25)$$

This is reminiscent of the Fermat principle in optics but applied here within an heterogeneous medium characterized by the flow $\mathbf{U}$.

Given the selected trajectory $\mathcal{T}(\tilde{p})$, the effective front velocity will simply read

$$V_f = \frac{L}{T(\tilde{p})}. \quad (26)$$

The remainder of this article is devoted to work out this model and to validate it from the experiment.

VI. OPTIMIZATION MODEL FOR FRONT PROPAGATION

For the sake of simplicity, we consider hereafter square vortex cells. Extrapolation to the rectangular cells involved in the experiment is performed in Appendix D.

A. Family of trajectory and flow modelization

The first step of the modeling consists in defining a relevant family of trajectories for the leading point M of the front defined as its most advanced point on the mean direction of propagation $\mathbf{e}_x$. Following Fig. 1, we consider two phases of motion: the slow crossing of a vortex separatrix and the quick advection towards the next separatrix.

When crossing the separatrix, the leading point M can hardly be situated along the y axis since the front is nearly aligned on this direction. As shown in Fig. 13, it however advances at the laminar velocity V_o on the mean direction $\mathbf{e}_x$, in agreement with relation (24) since $\mathbf{U}\cdot\mathbf{n}=0$ there. Accordingly, we shall model its trajectory as a straight segment S located on the x axis and crossed at constant velocity V_o [Fig. 18(a)].

At the end of the above motion, the front takes advantage of flow advection to quickly transport itself to the next separatrix (Figs. 1 and 11). It then follows a curved path that is evidenced by the curved tongue it leaves behind. As the flow velocity U is large compared to the proper front velocity V_o, this motion mainly results from flow advection along the flow streamlines. Leaving aside the fine geometrical details of streamlines (Figs. 8 and 15), we shall model them as circles centered on the center of the square cell and assume that the trajectory of the leading point M of the front corresponds to one of the half-circles joining the straight paths S [Fig. 18(a)]. As the front tip rotates along this trajectory so as to always display a normal $\mathbf{n}$ aligned with the trajectory tangent $\boldsymbol{\tau}$ (Fig. 8 and 11), one has $\mathbf{U}\cdot\mathbf{n}=U$. Following Eq. (24), we shall thus attribute to point M a velocity $\mathbf{V}_M$ tangent to the streamlines and whose intensity is V_o+U: $\mathbf{V}_M=(V_o+U)\boldsymbol{\tau}$.

We obtain this way the trajectory sketched in Fig. 18(b). It is parametrized by the length of the straight path S taken to cross the separatrix or, equivalently, by the radius r of the circular trajectory. The trajectory of the leading point of the front thus belongs to a family of trajectories $\mathcal{T}(r)$ among which the optimal trajectory $\mathcal{T}(\tilde{r})$ has to be selected.

As the flow streamlines are taken circular, incompressibility implies that the flow intensity remains constant on them: $U\equiv U(r)$. To clarify its variation with r, it is convenient to consider the flow vertical vorticity Ω_z. Its sources are located at the magnet boundaries where the magnetic field suddenly reverses direction (Fig. 3). The vertical vorticity is then advected by the flow and diffused in the fluid until a steady state is reached. As $(\mathbf{U}\cdot\boldsymbol{\nabla})\Omega_z=U(r)\partial\Omega_z/\partial\theta=0$ on circular streamlines, steadiness in the bulk is obtained when vorticity no longer diffuses: $\Delta\Omega_z=0$. In the Hele-Shaw regime, this yields a constant vertical vorticity domain beyond a boundary layer of the order of half the cell depth. This corresponds, in the bulk, to a flow intensity varying linearly with the distance to the center, i.e., to a solid rotation: $U(r)\equiv\Omega_z r/2$.

This flow structure is valid until entering the boundary layers formed at the channel sides. Then, the flow intensity decreases to zero on a boundary layer depth Δ that is expected to be small compared to the cell size L. To account for this quick vanishing, we complete the above variation of flow intensity with a power-law variation of $U(r)$ with the distance $L/2-r$ to the boundary.

Denoting with a prime the spatial variables rendered nondimensional by $L/2$, we then obtain with $r'=2r/L$ the following flow structure:

$$U(r)=\hat{U}r'(1-r')^c, \tag{27}$$

where c stands for an exponent that drives the structure of the boundary layer and $\hat{U}$ for a dimensionalization factor.

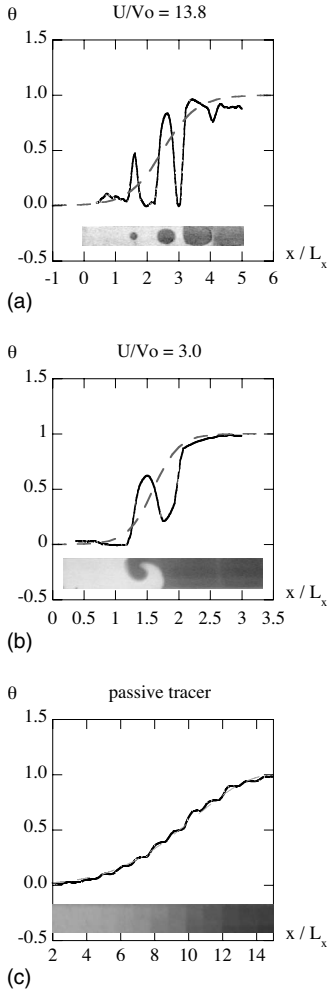

FIG. 17. Plot of the grey levels of front images as a function of the longitudinal coordinate x. Pictures are taken from three different experiments. (a) Propagating front at $U/V_o=13.8$, $V_f/V_o\approx 7.2$. (b) Propagating front at $U/V_o=3.0$, $V_f/V_o=2.7$. (c) Effective diffusion of a passive tracer in a chain of twenty convective rolls. Solid lines correspond to the average grey levels on the y direction, $\bar{\theta}(x,t)$, and dashed lines to the traveling wave profile $\langle\theta\rangle(x,t)$.

The maximum flow velocity $\bar{U}$ is obtained for $r'=(1+c)^{-1}$ at a relative location δ' that we define as the beginning of the boundary layer (Fig. 19).

$$\delta'=2\delta/L=(1+c)^{-1}, \tag{28}$$

$$\bar{U}=U(\delta')=\hat{U}\delta'(1-\delta')^{\delta'^{-1}-1}. \tag{29}$$

Although this flow does not fit the straight boundaries, it corresponds to a relevant modeling of viscous vortices in the region where the trajectories $\mathcal{T}(r)$ actually belong. It thus provides a flow model to a sufficient level of details for the present purpose. It is parametrized by a *single* parameter, the relative location δ' of the flow boundary layer in the cell.

Although the parameter δ' is *a priori* free here, it is actually prescribed in our experiment to a value fixed by the geometry. This results from the fact that the hydrodynamical regime is a Hele-Shaw regime in which the lateral boundary

layer thickness Δ is fixed to the half cell depth: $\Delta \approx d/2$ (Sec. IV F). This makes $\delta' = (L/2 - \Delta)/(L/2)$ prescribed by the vortex aspect ratio d/L:

$$\delta' \approx 1 - d/L. \tag{30}$$

Within the Hele-Shaw regime in which our experiment stands (Sec. III C), the optimization model therefore relies on *no* free parameter.

B. Fastest trajectory and effective velocity

The competition between trajectories regarding their propagation time in a vortex is qualitatively illustrated in Fig. 18(c) on three particular trajectories, at small, intermediate and large distance to the vortex center. Their total length increases since the decrease of paths S is overcompensated by the increase of the curved path C. On the other hand, the flow intensity on them first increases with the distance to the vortex center but then decreases as the boundary is approached. This finally results in a short but slow trajectory at small r, a longer and quicker trajectory at intermediate r, and a still longer but slower trajectory at large r. This obviously provides a least propagation time for some intermediate trajectory that is accurately selected below.

The travel time $T(r)$ through a cell reads

$$T(r) = \frac{L - 2r}{V_o} + \frac{\pi r}{U(r) + V_o}. \tag{31}$$

Given the flow structure (27), the least time criterion $dT/dr = 0$, $d^2T/dr^2 > 0$ (25) provides an implicit relationship on the optimal trajectory $r = \tilde{r}$,

$$\left(\frac{dU}{dr}\right)_{\tilde{r}} = -\left[\frac{2}{\pi}\left(\frac{U(\tilde{r})}{V_o}\right)^2 + \left(\frac{4}{\pi} - 1\right)\frac{U(\tilde{r})}{V_o} + \left(\frac{2}{\pi} - 1\right)\right]\frac{V_o}{\tilde{r}}. \tag{32}$$

Selection of the optimal trajectory $\mathcal{T}(\tilde{r})$ can then be achieved by plugging into this relation the explicit expressions of the flow intensity (27) and of its gradient

$$\left(\frac{dU}{dr}\right)_{\tilde{r}} = \hat{U}(1 - \tilde{r}')^{c-1}\left(1 - \frac{\tilde{r}'}{\delta'}\right)\frac{2}{L}, \tag{33}$$

where $\tilde{r}' = 2\tilde{r}/L$ and $\delta' = 2\delta/L$.

Even for the simple expression (27) of $U(r)$, the above scheme yields no explicit expression for the location $\tilde{r}$ of the optimal trajectory and thus, for the effective front velocity V_f. Such a determination may nevertheless be obtained within some approximations of the above relationships. In particular, dropping out the two rightmost terms of relation (32) yields an approximation of the intensity gradient that is better than 10% even at small values of $U(\tilde{r})/V_o$ (Fig. 20),

$$\left(\frac{dU}{dr}\right)_{\tilde{r}} = -\frac{2}{\pi}\left(\frac{U(\tilde{r})}{V_o}\right)^2 \frac{V_o}{\tilde{r}}\left[1 + O\left(\frac{V_o}{U(\tilde{r})}\right)\right]. \tag{34}$$

Comparison between this approximate relation and relation (33) then yields the following selection of the optimal trajectory:

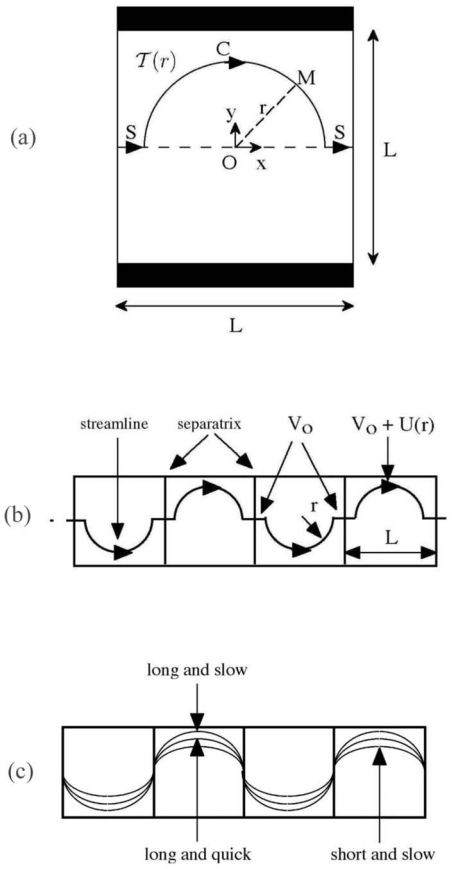

FIG. 18. Front trajectory model. (a) Front trajectory $\mathcal{T}(r)$ within a square cell. It is made of two straight paths S enclosing a circular path C. (b) Front trajectory in the channel. The front velocity is V_o on straight paths S since there is no flow advection on them. It is $V_o + U(r)$ on curved path C since the front normal is then tangent to the trajectory which is also a streamline. (c) Sketch of the competition between trajectories. Three trajectories are considered at small, intermediate, and large distance r to the vortex center. The first trajectory is short but slow; the second is longer but quicker; the last is longer and slower. The optimal trajectory thus stands in between, around the intermediate trajectory.

$$1 - \tilde{r}' = \left[\frac{\pi}{2}\frac{(1 - \delta') - (1 - \tilde{r}')}{\delta'\tilde{r}'}\frac{V_o}{\hat{U}}\right]^{\delta'}. \tag{35}$$

Following Eq. (34), the gradient of the flow intensity is negative on the optimal trajectory. This, according to Eq. (33), implies that the optimal trajectory is located in the boundary layer $\delta' < \tilde{r}' < 1$ (Fig. 19). Relation (35) then shows that the optimal trajectory quickly goes closer to the boundary as the velocity $\hat{U}$ is increased. This allows approximating $\tilde{r}'$ by 1 in the right-hand side of Eq. (35) to obtain at the dominant order in the relative velocity $\hat{U}/V_o$,

$$1 - \tilde{r}' = \left[\frac{\pi}{2}\left(\frac{1}{\delta'} - 1\right)\frac{V_o}{\hat{U}}\right]^{\delta'} + o\left[\left(\frac{V_o}{\hat{U}}\right)^{\delta'}\right]. \tag{36}$$

The optimal trajectory being determined, relations (26), (27), and (31) now provide the flow intensity on it and the resulting effective front velocity,

$$\frac{U(\tilde{r})}{V_o} = H\left(\frac{\hat{U}}{V_o}\right)^{\delta'} - G, \tag{37}$$

$$\frac{V_f}{V_o} = \frac{1 - G + H\left(\frac{\hat{U}}{V_o}\right)^{\delta'}}{\frac{\pi}{2} + G - K\left(\frac{\pi}{2} + G - 1\right)\left(\frac{\hat{U}}{V_o}\right)^{-\delta'}}, \tag{38}$$

with $G=\pi/2(1/\delta'-1)$, $H=G^{1-\delta'}$, and $K=G^{\delta'}$.

In terms of the maximal flow intensity $\bar{U}=U(\delta')$ (29), the explicit expressions of the relative location of the optimal trajectory and of the optimal effective front velocity finally read

$$\tilde{r}' = 1 - (1-\delta')\left(\frac{2}{\pi}\frac{\bar{U}}{V_o}\right)^{-\delta'}, \tag{39}$$

$$\frac{V_f}{V_o} = \frac{1 - (1-\delta') - \left(1 - \frac{2}{\pi}\delta'\right) + \left(\frac{2}{\pi}\frac{\bar{U}}{V_o}\right)^{\delta'}}{1 - (1-\delta')\left(1 - \frac{2}{\pi}\delta'\right)\left(\frac{2}{\pi}\frac{\bar{U}}{V_o}\right)^{-\delta'}}. \tag{40}$$

Besides the apparent complexity of this relationship, the effective front velocity in a channel simply appears to depend on a *single* variable, the relative flow velocity $\bar{U}/V_o$, *and* a *single geometric* parameter, the relative boundary layer thickness δ'. In particular, the geometrical nature of exponent δ' is enforced here by its independence on the flow intensity $\bar{U}$, as a result of the forcing of the boundary layer thickness to half the cell depth in the present Hele-Shaw regime (30). Then, the asymptotic trend of the effective velocity V_f with the flow intensity $\bar{U}$ appears to be a power law,

$$\bar{U}/V_o \gg 1 : V_f/V_o \approx (2\bar{U}/\pi V_o)^{\delta'}, \tag{41}$$

whose exponent δ' is not constant but *dependent* on the *geometric* features (d,L) of the medium in which the front propagates (30).

C. Sensitivity to front trajectory and model parameters

Beyond the determination of the fastest trajectory, it is instructive to address the sharpness of its selection. This comes about investigating, for a fixed $\bar{U}/V_o$, the sensitivity of the relative effective front velocity V_f/V_o displayed on a given trajectory $\mathcal{T}(r)$ to the variations of its main parameters: the relative location δ' of the boundary layer and the relative position r' of the trajectory.

At fixed values of $\bar{U}/V_o$ and δ', the variation of V_f/V_o with the trajectory shows a sharp peak which culminates at the fastest trajectory. An example of this is displayed in Fig. 21(a) for $U/V_o=10$ and $\delta'=0.78$. Here, a drift of only $\delta r' = +3\times10^{-2}$ or -10^{-1} of the location of the trajectory from its optimal position $\tilde{r}'$ results in a drop of the effective velocity of 25%. This large sensitivity may be understood as the consequence of the proximity of the quickest trajectory ($\tilde{r}'=0.96$, $V_f/V_o=5.5$) to the slowest trajectory ($\tilde{r}'=1$, $V_f/V_o=1$). It *a posteriori* justifies the need of a multitrajectory model to finely select the fastest trajectory for front propagation in this heterogeneous medium.

A visual consequence of the large sensitivity of front propagation to the trajectory is given by the tongue made by a front entering a vortex (Figs. 1, 14, 8, and 15). In particular, its thin digit form contrasts with the straight shape of the contaminated separatrix from which it has come about. This results from the differential effect of the velocity gradient on the trajectories of front points. In particular, those that are slightly shifted from the optimal trajectory show a noticeably reduced velocity (Fig. 21), following which the resulting envelope is digit shaped.

Still at a fixed value of $\bar{U}/V_o$, the effective front velocity V_f/V_o involved on the optimal trajectory displays noticeable variations with the thickness of the boundary layer [Fig. 21(b)]. Here the value $\delta'=1$ corresponds to no boundary layer and thus to free boundary conditions, as considered in one-trajectory models [18–20]. However, increasing the boundary layer thichness so that $\delta'=0.75$, as expected here for $L_y=12$ mm, drops V_f/V_o by as much as 40%. This stresses the importance of the subscales L_s of the flow (Fig. 16) on the efficiency of front propagation and thus the need for handling realistic boundary conditions in modeling.

VII. VALIDATION OF THE OPTIMIZATION MODEL

We compare below the predictions of the multitrajectory model to the experimental data. In particular, we focus attention on the variations of the reduced effective velocity V_f/V_o and of the relative location $\tilde{r}'$ of the fastest trajectory with the reduced flow velocity $\bar{U}/V_o$. For the sake of homogenity of the notations in the literature, we shall return hereafter to the notation U for the maximal flow velocity $\bar{U}$.

Whereas the multitrajectory model has been worked out in a square cell for the sake of simplicity, the present experiments have been performed in rectangular cells. However, the same kind of optimization can be easily worked out on them, once the family of trajectories and the flow structure are prescribed (Appendix D). In particular, guided by front observation and by symmetry considerations, we consider the same kind of trajectories as those used in square cells, the circular path being simply replaced by an elliptical path in rectangular cells. The flow intensity on these streamlines is deduced from that adopted in square cells by an affine and volume-preserving transformation. This yields a selection of the optimal trajectory (D10) and of the optimal effective front velocity (D11) that is similar to that discussed in a square cell, the relationships being simply parametrized by the ellipse excentricity.

A. Effective front velocity for the measured values of the boundary layer thickness

Observations of the tongues made by front propagation in the vicinity of the cell boundary have revealed that the loca-

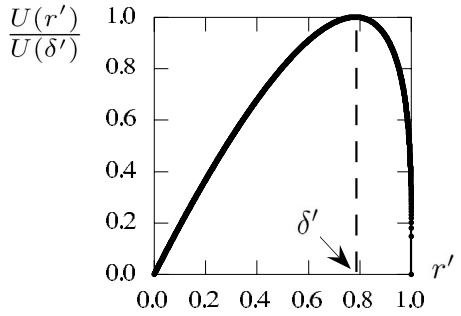

FIG. 19. One-parameter model for flow velocity in a square cell (27) with $c=0.28$. The rigid rotation near the cell center ends up at $r'=\delta'=0.78$ at a boundary layer.

tion of the fastest streamline is mostly independent of the flow velocity and simply prescribed by the cell depth d in the present Hele-Shaw regime: $\delta'=1-d/L_y$ (Sec. IV F) (30). In particular, measurements give the following range for δ' (Sec. IV F): $0.70<\delta'<0.85$ in the $(L_x,L_y,d)=(20,12,3)$ mm cell and $0.50<\delta'<0.60$ in the $(L_x,L_y,d)=(20,6,3)$ mm cell.

Figure 22(a) compares for the $(L_x,L_y,d)=(20,12,3)$ mm cell the experimental data on reduced effective front velocities and reduced flow intensities to the predictions of the multitrajectory model. It appears that data lay well within the channel delimited by the bounds given by the minimum (0.70) and the maximum (0.85) values measured for δ'. We stress that, once δ' is measured, there remains *no adjustable* parameter for the model, so that the observed agreement is valuable. It especially attests of the relevance of the multitrajectory model and of the selection by optimization. In particular, following Sec. VI C and Fig. 21(a), the effective velocity would drop down by 25% on a trajectory that would be off-selection by only 3% to 10% in relative location r'. If this had been the case, data would have missed the above channel.

To further test the role of the boundary layer thickness, i.e., of δ', in the selected effective velocity, we now address front propagation in the twice thinner channel: $(L_x,L_y,d)=(20,6,3)$ mm. Then $\delta'=1-d/L_y$ is expected to be 0.5, a value noticeably different than before since it corresponds to doubling the relative size of the boundary layer. Direct observations gave $\delta'=0.55\pm0.05$ in agreement with the expected value. Figure 22(b) here too provides data in agreement with the predicted bounds derived for the extreme values of δ'. In view of the sensitivity of the selected effective velocity to the boundary layer thickness [Sec. VI C and Fig. 21(b)], this corroborates the relevance of the optimization multitrajectory model.

B. Optimal value for the boundary layer thickness

Although the optimization model agrees with experiment with no adjustable parameter, it is instructive to consider the optimal values of the parameters that would give the best fit to data. This, in particular, will enable us to further judge the relevance of the model by comparing the shape of the best relationship it can propose to that displayed from measurements.

The values of δ' that yield the best agreement between the data and models are $\delta'_{opt}=0.78L/2$ in the large cell ($L_y=12$ mm) and $\delta'_{opt}=0.56L/2$ in the thin cell ($L_y=6$ mm). In both cases, Fig. 22 shows an excellent agreement with data regarding both the general trend and the curvature of the model curves. This supports the relevance of the model and gives confidence in its validity at larger flow intensities.

C. Selection of the fastest trajectory

The fastest trajectory can be identified as that of the front tip during its first advection towards the next boundary (Fig. 23). Its location may then be accurately determined provided it stands far enough from the boundary. In practice, this bounds its determination to moderate values of the flow intensity, $U/V_o<10$.

Figure 24 compares the experimental measurements made in the large and thin cells to the prediction of the model for the optimal value of parameter δ'. Although they are limited to moderate flow intensity, they reveal a good agreement between modeling and experiment, at least regarding the general trend. In particular, data and model agree on the rate at which the optimal trajectory is closer to the boundary as the flow intensity is increased. That this agreement is obtained for two optimal boundary layer thicknesses $\delta'\approx0.78$ and $\delta'\approx0.56$ in large and thin cells here too corroborates the relevance of the optimization model.

The fact that the fastest trajectory moves to the boundary as the flow intensity is increased while the fastest streamlines remains at the same location, finely illustrates the balance that the front has to optimize. Trajectories are made by a straight but slow path followed by a curved but quick path (Fig. 18). Both are coupled by the fact that one path shortens as the other lengthens. What balance is the most efficient to improve propagation as the flow intensity varies? The answer given by the optimization model is that the slow straight path must shorten in favor of the quick curved path as the flow intensity is increased, in a way that is precisely identified in relation (39) and Fig. 24.

VIII. DISCUSSION

The experimental study and the modeling reported above provide several insights into the mechanism of front propagation in stirred media, in particular regarding the nature of the effective propagation seen at a scale large compared to the vortex scale and the practical implications that may result from its main features.

According to the homogenization theories proposed at small Damköhler numbers, the effective front propagation should be viewed as an effective reaction-diffusion wave with coefficients renormalized by the flow intensity [17–19]. In this picture, the major effect of the flow is to enhance the diffusion properties and the reaction rate of the medium without changing the nature of the front propagation seen at a large scale. In particular, the effective front profile stands as a solution of a reaction-diffusion equation in which the vortex array no longer enters. In the frame comoving with the effective front, it thus corresponds, as for laminar fronts,

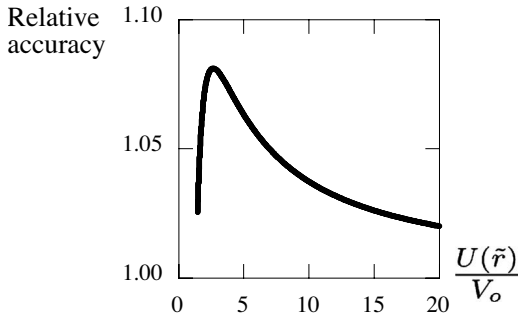

FIG. 20. Relative accuracy of the flow gradient approximation (34). The ratio of the velocity gradient approximated by relation (34) to its exact determination (33) is plotted as a function of the relative flow intensity $U(\tilde{r})/V_o$. The approximation is uniformly better than 10%.

to an equilibrium throughout the *whole* medium between an advection flux, a diffusion flux, and a source term. This provides for either lengths or velocities a *single* characteristic scale based on the renormalized values of the diffusion and reaction coefficients. Up to prefactors linked to the form of the effective reaction rate (Sec. II A), these scales then determine the wake length and the effective front velocity from *global* properties of the medium.

In contrast, we find here that, at large Damköhler numbers, the various front parts that are embedded in the front wake *do not interact* with their neighbors, since they are separated by fully burnt zones (Figs. 1 and 14). In particular, as these zero-gradient zones prevent diffusive flux in between cells, they deny a reaction-diffusion modeling for the effective front. As a confirmation, the concentration profiles show large subscale fluctuations at the vortex scale superimposed to the large scale wake profile (Fig. 17). This emphasizes the essential role of the vortex structure in the effective front propagation. In particular, the effective front velocity is set by the ability of the foremost part of the front to cross the next vortex separatrix, independently of the status of the remaining front parts. It thus stands on *local* properties of the medium.

Whereas in both cases the effective front seen at a large scale corresponds to a propagative signal, the phenomena that determine its form and its velocity largely differ. They correspond in the former case to an equilibrium between fluxes all over the medium and, in the latter case, to the independent dynamics of disconnected parts of the front. The nature of front propagation is then nonlocal in the former case and local in the latter case. Loosely speaking, it thus corresponds to a wave in the former case and to a particle followed by its wake in the latter case. Interestingly, front propagation depends much more sensitively on the fine structure of the flow in the latter local dynamics than in the former nonlocal dynamics.

Taking into account this analysis, we have developed a suitable modeling for describing the dynamics of the foremost front part. It corresponds to a particle moving at its proper velocity V_o and advected by the flow beyond some distance to the vortex separatrix (Fig. 18). This is similar to propagation in heterogeneous media, the heterogeneity being given here by flow advection. To remove the indeterminacy

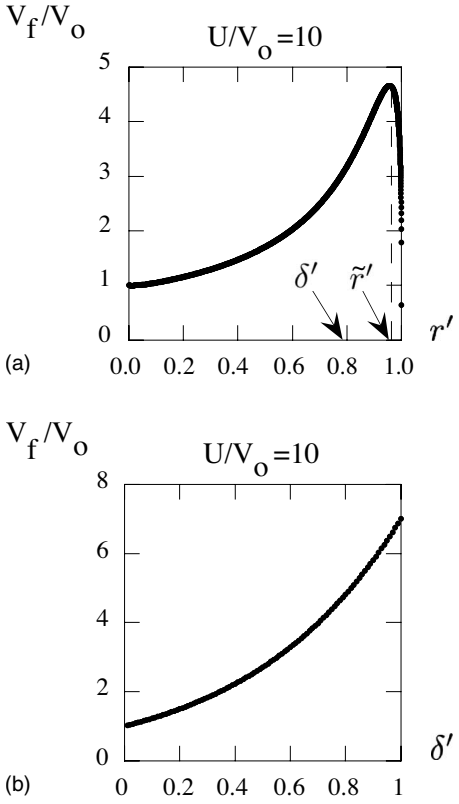

FIG. 21. Relative front velocity V_f/V_o given by the optimization model. (a) Evolution of the relative front velocity with the trajectory r', the remaining parameters and variables δ' and $\bar{U}/V_o$ being fixed at $\delta'=0.78$ and $U/V_o=10$. The largest velocity is the optimal front velocity. It is reached on the optimal trajectory $\tilde{r}'$. (b) Evolution of the optimal front velocity with the relative location δ' of the boundary layer at fixed $U/V_o=10$. A change of δ' from 1 (no boundary layer) to 0.75 (boundary layer thickness equal to a quarter of the distance to the cell center) makes the relative front velocity drop from 40%. This stresses the importance of the subscales L_s of the flow in the front propagation efficiency.

in the streamline followed by the particle, we have looked for the fastest trajectory among a family. This corresponds to a least-time criterion reminiscent of the Fermat principle in homogeneous media but applied here to heterogeneous situations.

As this criterion relies on optimization, it is thus sensitive to the details of the flow structure, especially its boundary conditions. In particular, front dynamics appears to depend on an hydrodynamic scale, the boundary layer thickness. However, in the present Hele-Shaw regime of the experiment, this scale is fixed to a geometric scale, the channel width, so that the model no longer involves any free parameter. It nevertheless provides, for two different aspect ratios, an excellent agreement between predictions and measurements regarding front velocity (Fig. 22), front trajectory (Fig. 24), and front wake (Fig. 14). This has been confirmed by the closeness of the measured boundary layer thickness (Fig. 8) to both its optimal value within the model (Fig. 22) and the half cell depth value expected in the present Hele-Shaw regime.

The dependence of the measured effective front velocity on the boundary layer thickness points out the specificity of

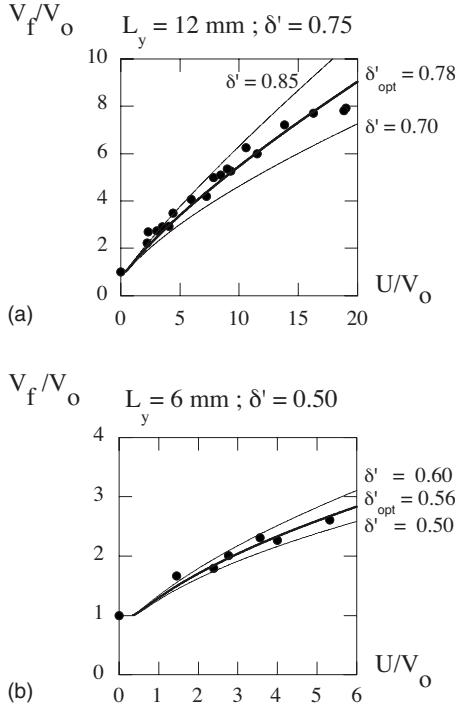

FIG. 22. Reduced effective velocity V_f/V_o as a function of reduced flow intensity U/V_o. Points correspond to data and lines to the effective velocities predicted by the model at different values of the parameter δ'. Without any adjustable parameter, data fit well with the predicted values for δ' belonging to its measurement range. The best fit of the model to data shows an excellent agreement on the whole range of velocity. (a) Cell size $(L_x, L_y, d) = (20, 12, 3)$ mm. Measurements of the boundary layer thickness gave $0.70L/2 < \delta' < 0.85L/2$. The best fit to data yields $\delta' = 0.78L/2$. (b) Cell size $(L_x, L_y, d) = (20, 6, 3)$ mm. Measurements of the boundary layer thickness gave $0.50L/2 < \delta' < 0.60L/2$. The best fit to data yields $\delta' = 0.56L/2$.

the optimization model as compared to the renormalization models or the kinematics models. In particular, at large flow velocity, it yields a power-law dependence of V_f on U (41) with an exponent δ' *dependent* on the channel aspect ratio (30) (Fig. 22), $\delta' = 3/4$ for $(L_y, d) = (12, 3)$ mm and $\delta' = 1/2$ for $(L_y, d) = (6, 3)$ mm. In contrast, other models predict a *fixed* exponent, $\delta = 1/4$ for the renormalization models [17–19] and $\delta = 3/4$ for the kinematics models [19–21], *independently* of the channel geometry.

Another advantage of the optimization model is to provide a complete solution to the effective front propagation that contrasts with the uncertainty or the uncompleteness induced in previous kinematic models from the absence of trajectory selection [19,21] or from the arbitrary choice of a definite trajectory [20]. Considering a path located on separatrixes, Vladimirova *et al.* [20] found a lower bound for the effective front velocity that was only half the value observed in simulations. On the other hand, computing from simulations the mean reduction of flow intensity related to the distance of the actual trajectory to the cell boundaries, Abel *et al.* [19] and Cencini *et al.* [21] found a good agreement between model and simulations regarding the effective front velocity. However, this reduction coefficient or, equivalently, the mean position of the front trajectory, remained indeterminate from the modeling only. In comparison, the present optimization model offers a definite answer parametrized by the flow structure and the flow intensity.

The sensitivity of front propagation to flow structure stressed by the optimization principle raises two main issues. One concerns practical implications of front propagation in stirred media; the other addresses the robustness of the results and of the modeling reported here.

Regarding the former issue, front propagation appears extremely efficient in evidencing the fastest streamlines of flows, at least on a main part of the medium. This, in particular, is a specific property of fronts over passive scalars since the flow structure can hardly be distinguished from diffusive profiles. Applying it to microfluidic issues where flows are usually in a laminar Hele-Shaw regime would enable the flow structure to be easily deduced from the shape of propagating fronts. In particular, appropriate use of the least-time criterion should enable one to solve, in a way similar as that achieved here, the inverse problem of identifying the fastest flow streamline from the front trajectory.

Increasing the flow velocity in our experiment would make boundary layers separate and the flow escape the Hele-Shaw regime. Then, secondary flow would be generated, rendering the flow nonplanar and three dimensional (Appendix C). In particular, one may even expect the separatrix to break, thereby leading neighbor cells to be connected by a flow streamline. As this flow transition would induce large implications on the front velocity, front propagation would stand here too as a very efficient way to detect it.

To infer the nature of front propagation in these more complex three-dimensional flows, it is instructive to return to the nondimensional numbers that set the basis of the front modeling (Sec. II B, Fig. 2). As neither the Péclet number nor the Damköhler number change order of magnitude, the regime of front propagation should remain the same. Accordingly, the same kind of propagation mechanisms should be in order. In particular, front propagation should still be driven by the foremost part of the front, the actual trajectory being the quickest of all. The main difference with the propagation in planar flows would then simply stand in a larger geometrical complexity that could be handled in a way similar as in two dimensions here. Dedicated experiments are required to confirm this expectation or evidence a fundamental change in the propagation mechanism.

IX. CONCLUSION

We have investigated experimentally the propagation of a reactive front in a steady planar cellular flow. This has been achieved by using autocatalytic chemical fronts in aqueous solutions stirred by electromagnetic means. The experimental regime stood in the Hele-Shaw regime within which the flow remains planar and in the flamelet regime in which the front remains thin despite stirring. In particular, as the front thickness was thinner than the vortex scales, the inner structure of vortices was finely visited by the front and could thus influence propagation.

The form and the velocity of fronts within vortices, in between vortices, and in the front wake have been docu-

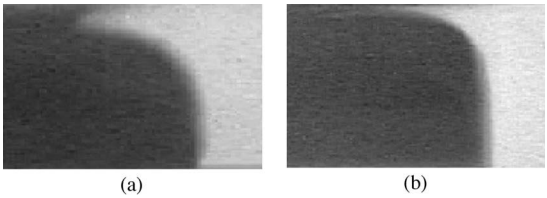

FIG. 23. Fastest trajectory evidenced from the front tongue displayed when entering a cell: (a) $U/V_o \approx 3$; (b) $U/V_o \approx 16$.

mented in the whole range of velocity within which the flow remains planar. Analysis of the regime of front propagation led us to reject a renormalized reaction-diffusion model for the effective front and turn attention to a more local, kinematic, modeling in which the dynamics of the foremost part of the front determines the velocity of the whole front wake. However, accurate determination of the effective velocity called for a fine identification of the actual trajectory followed by the leading point of the front. This has been achieved by selecting the fastest trajectory among a family suitably designed from observation.

The model involves a single parameter, the boundary layer thickness, and a single solution, the quickest trajectory. It provides a velocity depending not only on the relative flow amplitude but also on the flow geometry and the boundary conditions via the relative boundary layer location. However, in the Hele-Shaw regime pertaining to this experiment, the boundary layer thickness is prescribed by the cell depth as confirmed by direct observation. The model then no longer involves any free parameter. It is, however, found to compare very well to measurements, the effective velocity and the front trajectory being recovered with excellent agreement.

This optimization model corresponds to a least-time criterion analogous to the Fermat principle for light ray propagation but applied here to an heterogeneous medium made up by stirring vortices. Interestingly, it points to a sensitivity of the front trajectory and velocity to the flow structure, a property that could be useful for instance in microfluidic devices.

Although this study has taken place in planar flows, it has succeeded in pointing out a model of front propagation in structured flows whose physical basis, the least time criterion, is independent of the level of complexity of the flows or of the underlying medium. Accordingly, the resulting optimization model that expresses this criterion may be expected to also work, in suitable forms to clarify, in more complex flows (nonplanar or time-dependent) where it could have been more difficult to point out from the outset. Additional experiments are required to confirm this statement and state the range of validity of the least-time modeling to more complex but still structured flows.

APPENDIX A: FRONT PROPAGATION REGIMES

We analyze the different qualitative regimes that arise for front propagation in cellular flow. For the sake of clarity, attention is laid first on relative vortex size ξ and then on Péclet number Pe, the implications regarding the Damköhler number Da being deduced from relations (4) and (5). As a

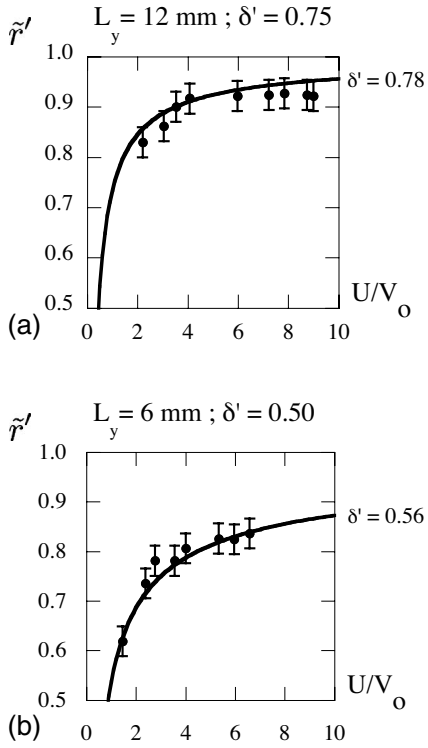

FIG. 24. Relative locations of the fastest trajectory. Full circles correspond to measurements from the tongues displayed by propagating fronts. Curves correspond to the predicted values from the optimization model (39) for values of δ' fitting the data the best (Fig. 22). (a) Cell sizes $(L_x, L_y, d) = (20, 12, 3)$ mm. (b) Cell sizes $(L_x, L_y, d) = (20, 6, 3)$ mm.

similar kind of analysis has been achieved in the combustion literature on fronts propagating in multiscale flows [52], we shall refer to the combustion terminology to depict the different regimes below.

1. Relative vortex size ξ

Small relative vortex size $\xi \ll 1$ corresponds to vortices small enough for possibly modifying the transport properties inside the front structure. We shall call this regime the *thin vortex regime* [Fig. 2(a)]. Depending on the flow intensity, it may result in an enhanced effective diffusion and thus, in an enlarged effective front thickness. Following this, we shall also call it *thick front regime*, even if the front will only be thickened at large flow intensity.

On the opposite, large relative vortex size $\xi \gg 1$ refers to vortices large enough for being viewed as uniform at the scale of the front thickness. Their advection effect can therefore be handled by a Gallilean frame change, so that the local front structure is expected to be unchanged. This is referred to as the *thick vortex regime* or the *thin front regime* [Fig. 2(a)].

2. Péclet number Pe

a. Pe$\ll$1.

In the small Péclet number regime, Pe$\ll$1, advection is too weak to make the advective transport more efficient than

the diffusive transport on the scale of a vortex, $\tau_a \gg \tau_d$.

However, for a small relative size of vortices, $\xi \ll 1$, diffusion on the vortex scale can be achieved before reaction is completed, $\tau_r \gg \tau_d$ (4), so that the transport process within the flame front can be modified. In particular, for $\xi \ll \mathrm{Pe}$, i.e., $\mathrm{Da} \ll g\ \mathrm{Pe}$ (4), vortex intensity is large compared to laminar front velocity, $U/V_o \gg 1$ (5), so that effective diffusion is enhanced at the vortex scale. This results in a thickened front called *thick flamelet* [Fig. 2(b)]. On the opposite, for $\mathrm{Pe} \ll \xi$, vortex intensity is small compared to laminar front velocity so that reaction dominates effective diffusion: the laminar front is recovered.

For a large relative vortex size, $\xi \gg 1$, the following hierarchy holds: $\tau_r \ll \tau_d \ll \tau_a$, Eqs. (4) and (5). This shows that diffusion at the vortex scale is preempted by reaction so that the laminar front is here also recovered. Notice that, following Eq. (4), this necessarily requires $\mathrm{Da} \gg 1$.

b. Pe≫1, Da≪1.

In the large Péclet number regime, $\mathrm{Pe} \gg 1$, the advective transport is more efficient than the diffusive transport at the vortex scale: $\tau_a \ll \tau_d$. This corresponds to usual experimental situations.

Small Damköhler numbers, $\mathrm{Da} \ll 1$, then refer to situations where advection at the vortex scale can take place before the corresponding medium has completed the reaction: $\tau_a \ll \tau_r$. Advection is then a transport phenomenon more efficient than reaction. In particular, mixing of species occur over a large number Da^{-1} of vortices before reaction can be significant.

In a thin vortex regime, $\xi \ll 1$, mixing is enhanced by diffusion, $\tau_d \ll \tau_r$, and is thus efficient in the whole vortices. One then expect a slow evolution of species concentration at the vortex scale L and thus an effective front with a thickness large compared to the vortex scale. We shall refer to this regime as the *well-stirred regime* [Fig. 2(b)]. Note that it necessarily corresponds to strong advection, $U/V_o \gg 1$.

In a thick vortex regime, $\xi \gg 1$, advection transports the front on the fastest streamlines on a large number of vortices while diffusion fails to transport it far in the interior of vortices, $\tau_d \gg \tau_r$. This results in a front extended on the periphery of many vortices and which exhibits a long wake. We shall refer to this as the *distributed reaction zone regime* [Fig. 2(b)].

c. Pe≫1, Da≫1.

Still in the large Péclet number regime, $\mathrm{Pe} \gg 1$, large Damköhler numbers $\mathrm{Da} \gg 1$ refer to advective flows slow enough for keeping reaction the quickest phenomenon: $\tau_r \ll \tau_a$. In particular, a fluid particle advected in a vortex fully reacts before having completed a turnover. This ensures that steep gradients of θ, i.e. a front, persist inside vortices despite advection. On the other hand, following Eq. (4), the relative vortex size is necessarily large, $\xi \gg 1$, so that the front structure keeps locally unchanged at a scale small compared to the vortex size. However, at a larger scale, the front is engulfed in vortices and wrinkled, so that its effective velocity V_f in the mean direction of propagation is enhanced. This kind of front, made by juxtaposition of front parts similar to a laminar front, is referred to as a *flamelet* in combustion. In particular, the front normal velocity is the same as in laminar conditions, provided that the weak corrections brought about by curvature are neglected. Then front propagation may be modeled as in geometrical optics by an eïkonal evolution with a constant normal velocity V_o. We shall refer to this regime as the *flamelet regime* [Fig. 2(b)].

APPENDIX B: DISCRETE AND CONTINUOUS INVARIANCE

To express the discrete and continuous invariances that are attached to effective propagation in the periodic vortex chain in a permanent regime, we introduce the average $\bar{\theta}$ of $\theta(x,y,t)$ in the y direction,

$$\bar{\theta}(x,t) = \int_{-L_y/2}^{L_y/2} \theta(x,y,t)\frac{dy}{L_y}. \tag{B1}$$

The periodicity of propagation in a permanent regime allows the definition of an effective velocity $V_f = L_x/T$, based on the vortex scale L_x and on the mean propagation time T through a vortex. Its existence reflects a discrete space-time invariance for the averaged profile $\bar{\theta}$,

$$\forall (x,t),\ \forall\, n,\ \exists\, (L_x,T);\quad \bar{\theta}(x+nL_x,t+nT) = \bar{\theta}(x,t) \tag{B2}$$

However, this discrete invariance does not extend to a continuous invariance, owing to the small scale structure brought about by the propagation inside a vortex.

To average out these subscales, we consider the spatiotemporal gliding average $\hat{\theta}$ of $\bar{\theta}$ along the characteristics $x(t) = x_o + V_f t$ of the mean motion and over a period (L_x,T),

$$\hat{\theta}(x,t) = \int_{-L_x/2}^{L_x/2} \bar{\theta}\left(x+u, t+\frac{u}{V_f}\right)\frac{du}{L_x}. \tag{B3}$$

Discrete invariance of $\bar{\theta}$ implies that the integral (B3) remains unchanged if integration is performed over a range $[-L_x/2+\tilde{u}, L_x/2+\tilde{u}]$ that is translated from the range $[-L_x/2, L_x/2]$ by an arbitrary shift $\tilde{u}$. This means that $\hat{\theta}(x,t)$ does not depend on the actual location of the range on which integration is performed but only on its length L_x. This translational invariance can be transformed into a continuous invariance of $\hat{\theta}$ by interpreting the *arbitrary* translation mode $\tilde{u} = V_f\tilde{t}$ as a combined shift $(V_f\tilde{t},\tilde{t})$ on space and time:

$$\forall (x,t),\ \forall\, \tilde{t},\ \exists\, V_f;\quad \hat{\theta}(x+V_f\tilde{t}, t+\tilde{t}) = \hat{\theta}(x,t). \tag{B4}$$

The averaged profile $\hat{\theta}$ then stands as a traveling wave whose nature, an actual wave or the wake of a propagating particle, is discussed in Sec. V A.

APPENDIX C: THE HELE-SHAW REGIME

The Hele-Shaw regime stands in narrow gap geometries at sufficiently low flow velocities. It corresponds to boundary

layers invading the whole fluid and thus, to a fully viscous regime. At larger velocities, it leaves place to a coexistence between viscid and inviscid domains which may yield specific hydrodynamic flows. Our goal here consists in determining the velocity threshold that bounds the Hele-Shaw regime in our experimental configuration and the hydrodynamic features that may come about beyond. We shall draw attention on a cell enclosing a steady vortex whose axis is parallel to the cell depth (Fig. 25).

We start from above the Hele-Shaw regime by considering, at large flow velocities, the coexistence between viscous boundary layers at the top and bottom plates and an inviscid zone in between (Fig. 26). We place the origin at the bottom boundary and we label ζ the boundary layer thickness, d the cell depth, and $\mathbf{V}(x,y,z)$ the flow. We note ρ the volumic mass of the fluid, μ its dynamic viscosity and ν its kinematic viscosity.

In the inviscid zone, flow advection on the curved vortex streamlines generates a centrifugal force that is balanced by a radial pressure gradient

$$\zeta \ll z < d/2; \quad \rho(\mathbf{V}\cdot\boldsymbol{\nabla})\mathbf{V} \sim \boldsymbol{\nabla}P \sim \frac{\partial P}{\partial r}\mathbf{e}_r. \tag{C1}$$

In the boundary layers that arise at the channel sides (Fig. 27), this pressure gradient persists but the centrifugal force weakens and eventually vanishes at the boundaries, together with the flow intensity. Force equilibrium then only involves a viscous force and the remaining pressure gradient. The former is proportional to the flow in the present narrow gap configuration and the latter is mainly radial,

$$0 < z \ll \zeta; \quad \boldsymbol{\nabla} P = \mu\Delta\mathbf{V} \sim \mu\frac{\partial^2\mathbf{V}}{\partial z^2}. \tag{C2}$$

As the primary flow is mainly orthoradial, it cannot compensate the radial component of the pressure gradient, so that a secondary radial flow is mandatory. Incompressibility then imposes a vertical back flow, and thus, an additional vortex in each of the half cell depth, in a way analogous to the generation of secondary flows on Eckman layers (Fig. 28) [42].

The occurence of an inviscid zone in between the boundary layers therefore implies not only a change of the flow profile but also a change of the flow structure which no longer remains planar. In particular, an advective transport process now takes place in the direction of the vortex center. Although its intensity is weak compared to the primary flow, it might be of paramount importance in the present problem, since it provides to the front the opportunity of quickly contaminating the whole vortex. To avoid handling different flow regimes, the present study has been performed so as to remain in the Hele-Shaw regime where no inviscid zone is in order.

The criterion which states the end of the Hele-Shaw regime is the occurrence of an inviscid zone when the two boundary layers fail to overlap. It corresponds to a boundary layer thickness ζ just equal to half the cell depth d: $\zeta \geqslant d/2$. To determine the corresponding velocity bound, we evaluate the boundary layer thickness ζ from the vorticity dynamics projected on the depth direction $\mathbf{e}_z$,

$$(\mathbf{V}\cdot\boldsymbol{\nabla})\Omega_z = (\boldsymbol{\Omega}\cdot\boldsymbol{\nabla})V_z + \nu\Delta\Omega_z. \tag{C3}$$

In the boundary layer, vortex stretching is weak, especially because the vertical flow is a secondary flow. Vorticity dynamics then mainly results from an equilibrium between vorticity advection and vorticity diffusion. Evaluation of both these terms may be performed using the characteristic scales of variations on the three space directions. These are $L_x/2$, $L_y/2$ on the x and y directions. However, the parabolic profile on the z direction yields a characteristic scale which is $\zeta/2$ at the boundaries but which diverges to infinity at the parabola summit (Fig. 29). We thus prefer evaluating this scale by considering the mean slope l over the domain under study [e.g., $\delta V(x,y,z)/\delta z = U(x,y)/l$, where $U(x,y)$ is the amplitude of the variations of V over the channel depth]. Drawing attention to a domain extending over the last part of the boundary layer, i.e., $\zeta' < z < \zeta$, we then obtain a scale $l = \zeta/\gamma$ with $\gamma = 1-\zeta'/\zeta$: $\frac{\partial}{\partial x} \sim \frac{1}{L_x/2}$, $\frac{\partial}{\partial y} \sim \frac{1}{L_y/2}$, $\frac{\partial}{\partial z} \sim \frac{\gamma}{\zeta}$. In particular, considering the second half of the boundary layer for appropriately determining its transition to the inertial zone yields $\zeta' = \zeta/2$ and $\gamma = 1/2$.

Applying these scalings gives, with $L_y < L_x$,

$$(\mathbf{V}\cdot\boldsymbol{\nabla})\Omega_z \sim \frac{V}{L_y/2}\Omega_z, \tag{C4}$$

$$\nu\Delta\Omega_z \sim \nu\frac{\partial^2\Omega_z}{\partial z^2} \sim \nu\frac{\gamma^2}{\zeta^2}\Omega_z, \tag{C5}$$

and, finally, with $(\mathbf{V}\cdot\boldsymbol{\nabla})\Omega_z \approx \nu\triangle\Omega_z$,

$$V \sim \frac{\gamma^2}{2}\frac{L_y\nu}{\zeta^2}. \tag{C6}$$

This velocity, consistent with the Karman scaling of the Eckman pumping problem, corresponds to that required to develop a boundary layer thickness ζ in a semi-infinite medium above a plate. Applying it for $\zeta = d/2$ provides an estimation of the velocity bound U_{HS} beyond which the boundary layers would detach one from the other, making the fluid escape the Hele-Shaw regime

$$U_{HS} \sim 2\gamma^2\frac{L_y\nu}{d^2}. \tag{C7}$$

For the present experiment where $d = 3$ mm, $\nu \approx 1$ mm^2 s^{-1}, and $\gamma \approx 1/2$, we obtain a limit to the Hele-Shaw regime at about $U_{HS} \approx 20$ mm mn^{-1} for $L_y = 6$ mm and $U_{HS} \approx 40$ mm mn^{-1} for $L_y = 12$ mm. The experiment always remained in this regime where the flow field can be considered as planar. This was confirmed by the absence of spiral transport of the front towards the vortex centers.

APPENDIX D: EXTENSION OF THE OPTIMIZATION MODEL TO RECTANGULAR CELLS

For the sake of simplicity, the optimization model has been worked out in Sec. VI on a square cell. We wish to

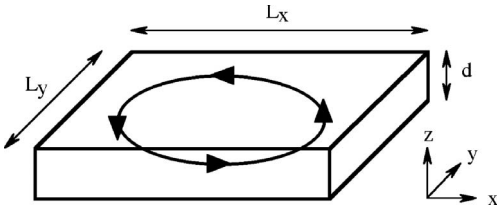

FIG. 25. Geometry of a cell enclosing a vortex.

extend it here to the rectangular cells involved in our experiment.

The first step consists in modeling the streamline geometry and the stream function in rectangular cells and in defining a family of trajectories for the front. For this, we shall take advantage of a simple geometrical, area-preserving, transformation linking squares to rectangles to extrapolate the flows and the trajectories modeled in square cells to those standing in rectangular cells. The next step will address the determination of the transit time T of the leading point of the front through a cell and the selection of the fastest trajectory. This will provide relationships similar to those obtained in square cells but parametrized by the rectangle aspect ratio.

For the sake of simplicity of the notations, the dimensions (L_x, L_y) of rectangular cell are denoted $(2a, 2b)$ and two lengths are introduced, $l=(ab)^{1/2}$ and $l'=(a^2/2+b^2/2)^{1/2}$. Notice that, in a square cell, the lengths l and l' would all be equal to half the square side L, $l=l'=L/2$.

1. Flow and trajectories

Rectangles of half dimensions (a,b) and squares of half dimensions (l,l) simply differ by an anisotropic dilation, i.e., by the affine transformation,

$$(x,y) \to (\breve{x},\breve{y}) = \mathcal{A}(x,y) = l\left(\frac{x}{a},\frac{y}{b}\right), \tag{D1}$$

where (x,y) [respectively, $(\breve{x},\breve{y})$] denote the rectangle (respectively square) coordinates. Interestingly, the affine transformation $\mathcal{A}(.,.)$ is area preserving. It thus actually map the incompressible flow in a rectangle onto an incompressible flow in a square. Taking, as in Sec. VI, circular streamlines for modeling flows in a square then yields elliptical streamlines in a rectangle whose equation is

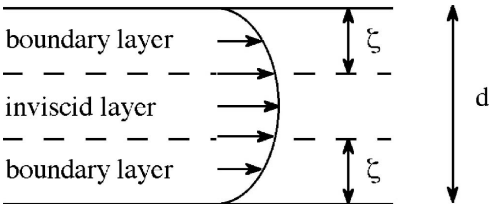

FIG. 26. Sketch of a cellular flow in the vertical plane. Two boundary layers of width ζ enclose an inviscid layer. In the Hele-Shaw regime, the boundary layers are so extended that they leave no room for an inviscid layer.

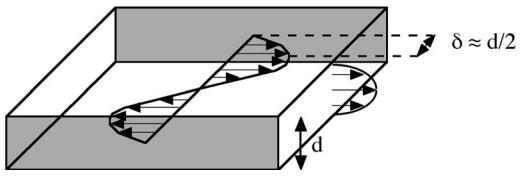

FIG. 27. Sketch of the flow components in the Hele-Shaw regime. Both vertical and horizontal boundary layers extend over half the cell depth.

$$\frac{x^2}{a^2}+\frac{y^2}{b^2}=\alpha^2, \tag{D2}$$

the label α being equivalent to the reduced radius $r'=r/l$ of circular streamlines with $r^2=\breve{x}^2+\breve{y}^2$.

In the same spirit as in Sec. VI, trajectories are modeled by a straight path on the x direction starting from a separatrix, followed by an elliptical streamline and ending with a second straight path at the next separatrix (Fig. 30). The front advances with the laminar velocity V_o on straight paths and with the flow velocity plus the laminar velocity on the elliptical path.

We call $\psi(\alpha)$ the stream function of the flow in the rectangular cell and $\breve{\psi}(r)$ the stream function of the flow in the corresponding square cell. The variations of either stream functions $\psi(\alpha)$, $\breve{\psi}(r)$ in between related trajectories corresponds to the elementary area scanned by the flow in its current tube per unit time. As areas are preserved by $\mathcal{A}(.,.)$, both variations are then the same: $d\psi=d\breve{\psi}$. Using the modeling (27) of the flow in a square and the relationship $\alpha=r'=r/l$, we obtain

$$\frac{d\psi}{d\alpha}=l\frac{d\breve{\psi}}{dr}=-l\hat{U}\alpha(1-\alpha)^c, \tag{D3}$$

with $c=l/\delta-1$, δ being the relative distance of the boundary layer to the cell center in the square cell (Sec. VI A, Fig. 19). This provides, in rectangular cells and in frame $(\mathbf{e}_x,\mathbf{e}_y)$, the following flow on elliptical streamlines

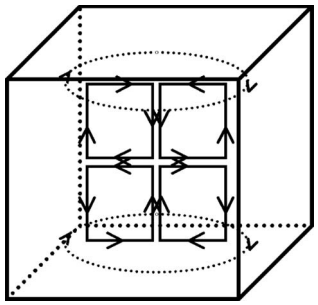

FIG. 28. Sketch of the secondary flows generated from a primary vortex flow by unbalanced radial pressure gradient in the boundary layers of a container.

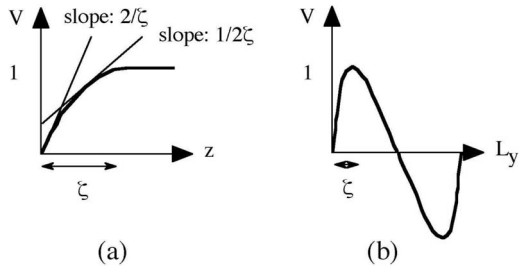

FIG. 29. Profile of the flow velocity $V(x,y,z)$ in the vertical plane (a) and in the horizontal plane (b). The maximal flow amplitude is normalized to unity. The slope of the profile in the vertical plane is $2/\zeta$ at the boundary and 0 at the end of the boundary layer. Its mean slope in the second half of the boundary layer, $1/2\zeta$, is then more relevant to express the equilibrium between vorticity advection and vorticity diffusion. It corresponds to a characteristic scale 2ζ for evaluating the transition to an inviscid zone.

$$\mathbf{U} = \frac{1}{l^2}\frac{d\psi}{d\alpha}\begin{bmatrix} -a\sin\varphi \\ b\cos\varphi \end{bmatrix} \tag{D4}$$

with φ defined by $x=\alpha a\cos(\varphi)$, $y=\alpha b\sin(\varphi)$.

2. Transit time, optimization, and selection

The advection time T_a of the leading point of the front on the half-ellipse $\mathcal{E}(\alpha)$ of a trajectory $\mathcal{T}(\alpha)$ reads

$$T_a(\alpha) = \int_{\mathcal{E}(\alpha)} \frac{ds}{U(\alpha,\varphi)+V_o}. \tag{D5}$$

Here s denotes the curvilinear abcissa and $U(\alpha,\varphi)$ the flow intensity at the location (α,φ), $U(\alpha,\varphi)=\hat{U}\alpha(1-\alpha)^c l(\varphi)/l$, where $l(\varphi)=(a^2\sin^2\varphi+b^2\cos^2\varphi)^{1/2}$. Introducing the average $\tilde{U}$ of the flow intensity on the streamline α yields $U(\alpha,\varphi)=\tilde{U}(\alpha)l(\varphi)/\langle l\rangle$ with

$$\langle l\rangle = \int_0^\pi l(\varphi)\frac{d\varphi}{\pi} = e^{-1/2}Jl, \tag{D6}$$

where e denotes the ellipse excentricity $e=a/b$ and $J=\int_0^\pi[1+(e^2-1)\sin^2(\varphi)]^{1/2}d\varphi/\pi$. Then

$$T_a(\alpha) = \int_0^\pi \frac{\alpha l(\varphi)}{\tilde{U}(\alpha)l(\varphi)/\langle l\rangle + V_o}d\varphi. \tag{D7}$$

A close approximation for T_a may be obtained by fixing $\varphi=\pi/4$ in the integrand of Eq. (D7). As $l(\pi/4)=l'$, this gives for the total transit time $T(\alpha)$ on streamline α,

$$T(\alpha) = \frac{2a}{V_o}(1-\alpha) + \frac{\pi\alpha l'}{G\tilde{U}(\alpha)+V_o}, \tag{D8}$$

where $G=e^{1/2}J^{-1}\,l'/l$.

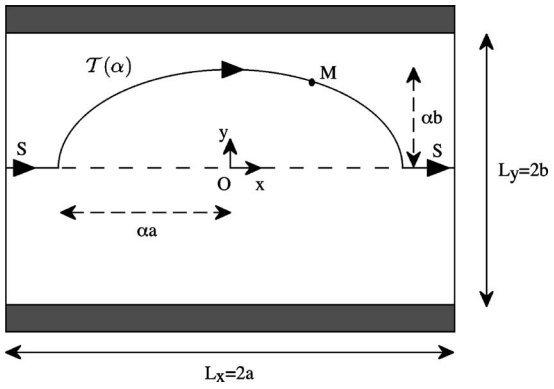

FIG. 30. Front trajectory within a rectangular cell. Trajectories $\mathcal{T}(\alpha)$ are made of two straight paths S and an elliptical path parametrized by α in between.

The optimal trajectory $\tilde{\alpha}$ is selected from Eq. (D8) by the least-time criterion $(dT/d\alpha)_{\tilde{\alpha}}=0$. As in a square cell (Fig. 20, Sec. VI B), it reads to a good approximation,

$$\left(\frac{d\tilde{U}}{d\alpha}\right)_{\tilde{\alpha}} \approx -\frac{e}{J}\frac{2}{\pi}\left(\frac{\tilde{U}(\tilde{\alpha})}{V_o}\right)^2\frac{V_o}{\tilde{\alpha}}.$$

As $\tilde{U}=e^{-1/2}J\alpha(1-\alpha)^c\hat{U}$, this gives

$$1-\tilde{\alpha} = \left[e^{-1/2}\frac{\pi}{2}\left(\frac{1}{\delta'}-1\right)\frac{V_o}{\hat{U}}\right]^{\delta'}, \tag{D9}$$

with $\delta'=\delta/l$. The effective front velocity then follows from $V_f=2a/T(\tilde{\alpha})$.

Using the maximal flow velocity $\bar{U}=\tilde{U}(\delta')$ to express the flow intensity, we obtain

$$\tilde{\alpha} = 1-(1-\delta')\left(f\frac{2}{\pi}\frac{\bar{U}}{V_o}\right)^{-\delta'}, \tag{D10}$$

$$\frac{V_f}{V_o} = \frac{1-(1-\delta')-\left(1-g\frac{2}{\pi}\delta'\right)+\left(f\frac{2}{\pi}\frac{\bar{U}}{V_o}\right)^{\delta'}}{1-(1-\delta')\left(1-g\frac{2}{\pi}\delta'\right)\left(f\frac{2}{\pi}\frac{\bar{U}}{V_o}\right)^{-\delta'}}, \tag{D11}$$

with $f=e/J$ and $g=a/l'$.

Taking $a=b$ turns out returning to a square cell. As expected, relations (D10) and (D11) then reduce to those initially derived in square cells (39) and (40) since $l=l'=a=L/2$, $\delta'=2\delta/L$, $e=J=1$, and $f=g=1$.

In practice, for the rectangular cells considered here, we have for $(L_x,L_y)=(20,12)$ mm, $e=5/3$, $J=1.354$, $f=1.23$, $g=1.21$, and, for $(L_x,L_y)=(20,6)$ mm, $e=10/3$, $J=2.327$, $f=1.43$, and $g=1.35$.

[1] *Oscillations and Travelling Wave in Chemical Systems*, edited by R. J. Field and M. Burger (Wiley, New York 1985).
[2] I. R. Epstein, Nature (London) **374**, 231 (1995).
[3] F. A. Williams, *Combustion Theory* (Benjamin-Cummings, New York, 1985).
[4] J. D. Murray, *Mathematical Biology* (Springer-Verlag, Berlin, 1989).
[5] E. R. Abraham, Nature (London) **391**, 577 (1998).
[6] E. R. Abraham, C. S. Law, P. W. Boyd, S. J. Lavender, M. T. Maldonado, and A. R. Bowie, Nature (London) **407**, 727 (2000).
[7] S. Edouard, B. Legras, F. Lefèvre, and R. Eymard, Nature (London) **384**, 444 (1996).
[8] J. Xin, SIAM Rev. **42**, 161 (2000).
[9] H. Berestycki, in *Nonlinear PDEs in Condensed Matter and Reactive Flows*, edited by H. Berestycki and Y. Pomeau, NATO Sciences Sciences Series C Vol. 569 (Kluwert, Doordrecht, 2003).
[10] R. Borghi and M. Champion, *Modélisation et théorie des flammes* (Technip Editions, Paris, 2000).
[11] A. Pocheau, Phys. Rev. E **49**, 1109 (1994).
[12] O. Cardoso and P. Tabeling, Eur. J. Mech. B/Fluids **8**(6), 459 (1989).
[13] Y. Pomeau, C. R. Acad. Sci., Ser. II: Mec., Phys., Chim., Sci. Terre Univers **301**, 1323 (1985).
[14] W. Young, A. Pumir, and Y. Pomeau, Phys. Fluids A **1**, 462 (1989).
[15] T. H. Solomon and J. P. Gollub, Phys. Fluids **31**, 1372 (1988).
[16] A. Pocheau and F. Harambat, Phys. Rev. E **73**, 065304 (2006).
[17] B. Audoly, H. Berestycki, and Y. Pomeau, C. R. Acad. Sci., Ser. IIb: Mec., Phys., Chim., Astron. **328**, 255 (2000).
[18] M. Abel, A. Celani, D. Vergni, and A. Vulpiani, Phys. Rev. E **64**, 046307 (2001).
[19] M. Abel, M. Cencini, D. Vergni, and A. Vulpiani, Chaos **12**, 481 (2002).
[20] N. Vladimirova, P. Constantin, A. Kiselev, O. Ruchayskiy, and L. Ryzhik, Combust. Theory Modell. **7**, 485 (2003).
[21] M. Cencini, A. Torcini, D. Vergni, and A. Vulpiani, Phys. Fluids **15**, 679 (2003).
[22] A. N. Kolmogorov, I. G. Petrovskii, and N. S. Piskunov, Moscow Univ. Math. Bull. (Engl. Transl.) **1**, 1 (1937).
[23] Ya. B. Zel'dovich and D. A. Frank-Kamenetzki, Acta Physicochim. URSS **9**, 341 (1938).
[24] W. V. Saarloos, Phys. Rep. **386**, 29 (2003).
[25] A. Goriely, Phys. Rev. Lett. **75**, 2047 (1995).
[26] R. G. Abdel-Gayed, D. Bradley, and F. K. Lung, Combust. Flame **76**, 213 (1989).
[27] A. Pocheau and D. Queiros-Condé, Phys. Rev. Lett. **76**, 3352 (1996).
[28] S. S. Shy, P. D. Ronney, S. G. Buckley, and V. Yakhot, *Twenty-Fourth International Symposium on Combustion*, Sydney (The Combustion Institute, Pittsburgh, 1993), pp. 543–551.
[29] M. Leconte, J. Martin, N. Rakotomalala, and D. Salin, Phys. Rev. Lett. **90**, 128302 (2003).
[30] J. A. Pojman, I. R. Epstein, T. J. MacManus, and K. Showalter, J. Phys. Chem. **95**, 1299 (1991).
[31] M. R. Carey, S. W. Morris, and P. Kolodner, Phys. Rev. E **53**, 6012 (1996).
[32] M. Bockmann and S. C. Muller, Phys. Rev. Lett. **85**, 2506 (2000).
[33] J. Martin, N. Rakotomalala, D. Salin, and M. Böckmann, Phys. Rev. E **65**, 051605 (2002).
[34] L. M. Pismen, Phys. Rev. Lett. **78**, 382 (1997).
[35] C. R. Chinake and R. H. Simoyi, J. Chem. Soc., Faraday Trans. **93**, 1345 (1997).
[36] L. Rongy and A. de Wit, J. Chem. Phys. **124**, 164705 (2006).
[37] G. Searby and J. Quinard, Combust. Flame **82**, 298 (1990).
[38] M. S. Paoletti and T. H. Solomon, Phys. Rev. E **72**, 046204 (2005).
[39] R. Kessler, J. Fluid Mech. **174**, 357 (1987).
[40] D. Mukutmoni and K. T. Yang, National Heat Transfert Conference, Minneapoli, 1987 (unpublished).
[41] D. Mukutmoni and K. T. Yang, J. Heat Transfer **115**, 360 (1993).
[42] T. H. Solomon and I. Mezic, Nature (London) **425**, 376 (2003).
[43] P. D. Kepper, I. R. Epstein, K. Kustin, and M. Orban, J. Phys. Chem. **86**, 170 (1982).
[44] D. M. Weitz and I. R. Epstein, J. Phys. Chem. **88**, 5300 (1984).
[45] O. Citri and I. R. Epstein, J. Phys. Chem. **91**, 6034 (1987).
[46] C. E. Dateo, M. Orban, P. D. Kepper, and I. R. Epstein, J. Am. Chem. Soc. **104**, 504 (1982).
[47] J. Boissonade and P. D. Kepper, J. Chem. Phys. **87**, 210 (1987).
[48] I. R. Epstein and K. Kustin, J. Phys. Chem. **89**, 2275 (1985).
[49] D. M. Kern and C. H. Kim, J. Am. Chem. Soc. **87**, 5309 (1965).
[50] J. D. Meeus and J. Sigalla, J. Chim. Phys. Phys.-Chim. Biol. **63**, 453 (1966).
[51] B. F. Edwards, Phys. Rev. Lett. **89**, 104501 (2002).
[52] R. Borghi, in *Recent Advance in Aerospace Sciences*, edited by C. Bruno and C. Casci (Plenum, New York, 1985), pp. 117–138.